Characterization of the Surface Oxidation Layer of Niobium

by

Saba Yasaei

Bachelor of Science, K. N. Toosi University of Technology (KNTU), 2018

A Thesis Submitted in Partial Fulfillment

of the Requirements for the Degree of

MASTER OF SCIENCE

in the Physics and Astronomy Department at the University of Victoria

Saba Yasaei, 2023

University of Victoria

All rights reserved. This thesis may not be reproduced in whole or in part, by

photocopy or other means, without the permission of the author.

Supervisory Committee

Characterization of the Surface Oxidation Layer of Niobium

by

Saba Yasaei

Bachelor of Science, K. N. Toosi University of Technology (KNTU), 2018

Supervisory Committee

Arthur Blackburn, Co-Supervisor

Physics and Astronomy Department

Rogério de Sousa, Co-Supervisor

Physics and Astronomy Department

Abstract

Niobium is widely used in quantum computing devices and charged particle accelerators, while it is in superconducting state. In these applications the niobium surface is subjected to very different electric field strengths and the performance of both is limited by losses that occur in the native oxide which inevitable forms on its surface. Current research indicates that these losses occur by a two-level system (TLS) mechanism either in the surface oxide layer, or at its interfaces. However, the exact physical location and microstructure of the sites that host the TLS are not known. To gain this knowledge, tools and techniques require development. Here, electron energy loss spectroscopy (EELS) in a high-resolution transmission electron microscope is used and extended through the use of model fitting. The developed technique allows localized thickness - composition parameters to be extracted from relatively low-density EELS data in a manner that reduces background and other systematic effects from consideration. Using this technique in future studies of the ~5 nm thick surface oxide layer will enable more reliable and rapid comparisons of oxide layers formed under differing conditions, which may thus have different loss characteristics. This in turn will help isolate the hosts of the loss mechanisms in these materials, and so drive performance improvements in niobium devices where energy loss on its surface is critical.

Table of Contents

Supervisory Committee ii

Abstract iii

Table of Contents iv

List of Tables viii

List of Figures x

Acknowledgments xv

Dedication xvi

Chapter 1: Introduction and Motivation for Research in Superconducting Niobium and Niobium Oxide (NbO_x) 1

1.1. Literature Review and Problem Statement 1

1.1.1. Superconductivity Physics and Applications 1

1.1.2 Superconductivity in Niobium 2

1.1.3 Importance of Defects in Superconductive Niobium and Niobium Oxide 6

1.1.4 Dielectric Loss and Quality Factor in Superconducting Devices 8

1.1.5 Conclusion of the Literature Review about Defects in Superconductive Niobium and Niobium Oxide (NbO_x) 10

1.2. Research Motivation and Scope 11

Chapter 2: Introduction to Electron Microscopy and Focused Ion Beam Instrumentation 13

2.1. Overview of Electron Microscopy 13

2.2. Overview of Focused Ion Beam (FIB) 15

2.3. Sample (Lamella) Preparation for Electron Microscopy using FIB 16

2.4. Overview of Electron Energy Loss Spectroscopy 18

Chapter 3: Niobium and Niobium Oxide (NbO_x) Sample Preparation and Electron Microscopy Characterization 25

3.1. Bulk Niobium Metal Source and Specifications 25

3.2. Various Treatments on Bulk Niobium Samples 27

3.3. Characterizing Crystallinity and Grain Size of Treated Bulk Niobium Samples using X-Ray Diffraction (XRD) 29

3.4. Preparing a Lamella Sample using Focused Ion Beam (FIB) 31

3.4.1. Depositing a Protective Gold Layer on Bulk Nb Samples using Physical Vapor Deposition (PVD) 32

3.4.2. Sample Preparation with Hitachi FB-2100 34

3.4.3. Sample Preparation with Helios SEM/FIB 39

3.5. Electron Microscopy Imaging and Spectroscopy on Lamella Sample 41

3.5.1. Transmission Electron Microscopy of Lamella Sample 42

Chapter 4: Electron Energy-Loss Spectroscopy (EELS) Results and Analysis 44

4.1. Introduction 44

4.2. EELS Signal Model 48

4.3. EELS Results and Data Processing 60

4.3.1. Electron Energy Loss Spectroscopy (EELS) of Lamella Sample 60

4.3.2. Data Preparation for Curve Fitting 64

4.3.2. Fitting Algorithm 68

4.3.3. Results of Fitting 73

Chapter 5: Conclusion 88

Bibliography 91

Appendix A - Characterizing Crystallinity and Grain Size of Treated Bulk Niobium Samples using X-Ray Diffraction (XRD) 99

Introduction to XRD 99

Experiment Specifications and Parameters 100

Appendix B - Energy Dispersive X-Ray Spectroscopy (EDS/EDX) of Bulk Sample 108

List of Tables

Table 1 - Elemental composition of the samples. Concentrations are given in ppm and the table headings identify the samples, which are as described in section 3.2. 26

Table 2 - Average crystallite size of the samples based on the average grain size extracted from the three main XRD peaks (39°, 56°, and 70°). 31

Table 3 – FIB beam settings used for the steps of lamella preparation. Lower condenser lens setting and larger aperture sizes produce greater beam current. 35

Table 4 – Volumetric density and peak normalized areal densities of Nb and O in the layers of our model. Peak normalization divides areal density by its maximal value. For Nb this is in the pure Nb layer, and for O this is in the NbO_2 layer. 51

Table 5 - Model parameters 59

Table 6 - Measurement parameters for dataset 1 and 2 61

Table 7 – Minimum MSE achieved with different algorithms for datasets 1 and 2 and fitting approach B. 72

Table 8 – Extracted average thicknesses from the datasets with approach A. Thickness entries in the table have the form *T* [*u*, *v*], where *T* is the mean thickness, *u* is the standard deviation of the means across all lines, and *v* is an error estimate on a single line, averaged over all lines. The average MSE is the mean over all lines of the mean squared error between the fitted curves and experimental data. 76

Table 9 - Summary of mean extracted thicknesses from the datasets for both approaches. Thickness entries in the table have the form T [u, v], where T is the mean thickness, u is the standard deviation of the means across all lines, and v is an error estimate on a single line, averaged over all lines (see Eqn. (4.10)). 81

Table 10 - Crystallize size of the samples at the major Nb peaks 107

Table 11 – Average crystallite size of the samples based on the average grain size extracted from the three main peaks (39°, 56°, and 70°). 107

List of Figures

Figure 1 - (a) An IBM quantum computer, mounted on the plate of its fridge cooling system, and (b) an SRF accelerator cavity. 5

Figure 2- SEM images of the main steps regarding TEM lamella preparation: (a) FIB digging; (b) border cut; (c) nanomanipulator welding; (d–f) lamella displacement; (g) support welding; (h) nanomanipulator detachment; (i) thinning; (j) lamella analysis with STEM. (Figure taken from [39]). 18

Figure 3 – Illustration of the electron beam interaction with a sample in a TEM. The electron beam (blue) enters the sample from the upper side and transfers energy to the outgoing modes shown with outgoing arrows. The emerging beam thus has less energy than the incoming beam. 20

Figure 4 – A typical EELS spectra for boron nitride. The vertical axis, labelled e^-, gives the number of electron counts. 21

Figure 5 - Background fitting and signal integration regions on a typical EELS sharp onset core-loss edge. Γ = background fit window; Δ = signal integration window; I_b = background intensity; I_k = signal intensity. 22

Figure 6 – Optical images of the prepared bulk niobium samples, showing approximately half of the sample covered with a gold protection layer. The samples are all approximately 15 mm wide. 28

Figure 7 - XRD spectra of the samples used in this study, inset with an enlarged view of the 002 peak. 30

Figure 8 - Hitachi FB-2100 Gallium focused ion beam machine in the Advanced Microscope Facilities at the University of Victoria. 34

Figure 9 – Lamella preparation steps: (a) removing surrounding material; (b) lamella undercut; (c) attaching the lamella to the probe; and (d) removing the connection to bulk sample. 36

Figure 10 – Optical micrograph of a 5 post Cu TEM half grid (field of view and grid width is 3 mm). 37

Figure 11 – SEM images of (a) flattened lift-out grid tooth, ready for welding, and (b - d) the lamella when welded to the grid, looking down the tooth (b) and from the side in (c, d). The scale bar units are μm. 38

Figure 12 - FIB images of the final polished lamella taken with the lowest possible ion beam current in the instrument. Views are (a, b) from above and the side (c, d), where (b) and (c) give enlarged views. 39

Figure 13 – SEM images of (a) the lamella cut, (b) lamella lift-out, (c) side view of final lamella and (d) top view of final lamella. 41

Figure 14 – BF-TEM images (200 kV) of the Nb, Au interface (a) magnification of 95 k (b) magnification of 410 k. 43

Figure 15 - Schematic of the layered structure of the NbO_x interface. 49

Figure 16 - (a) The underlying model of the areal density for approach A and (b) an example Gaussian that is convolved with the underlying model. 50

Figure 18 - Schematic illustrations of the cross-sections of (a) idealized lamella (b) actual lamella with an oxide layer on niobium part and contamination. 54

Figure 18 - Underlying model of the stochiometric ratio used in approach B. 58

Figure 19 - Overview of survey regions (ADF STEM images) for dataset 1 (left) and dataset 2 (right). The regions surveyed are highlighted by the green rectangles. 61

Figure 20 - Signal and background window for dataset 1. The upper panel shows the Nb edge on top and the lower panel shows the oxygen edge. 63

Figure 21 - Signal and background window for dataset 2. The upper panel shows the Nb edge on top and the lower panel shows the oxygen edge. 64

Figure 22 – Grayscale maps showing the relative areal densities of (a) Nb and (b) O for dataset 1 determined from the niobium M and oxygen K edges resepctively, and (c) a schematic image of interface. 65

Figure 23 – Plots of the peak normalized data related to the niobium and oxygen areal densities for dataset 1 and 2. 67

Figure 24 - (a) Dark field image (b) Secondary electron image from the EELS area showing carbon contamination. 68

Figure 25 - Fitting results with three algorithms: (i) trust region reflective (MATLAB 'lsqnonlin'), (ii) annealing method, and (iii) genetic algorithm. 72

Figure 26 – Sample fitting on the first two rows of the areal densities of oxygen and niobium for dataset 2. 75

Figure 27 – Example extracted thicknesses with the model fitting on dataset 1 with approach A. 75

Figure 28 – Example extracted thickness with the model fitting on dataset 2 with approach A. 76

Figure 29 – Fitted models for dataset 1 with approach B. 79

Figure 30 – Example extracted thickness with model fitting on dataset 1 with approach B. 79

Figure 31 – Fitted models for dataset 2 with approach B 80

Figure 32 – Example extracted thickness with the curve fitting on dataset 2 with approach B. 80

Figure 33 - Background-removed (a) Nb and O signals, (b) Nb:(Nb+O) ratio and (c) O:(Nb+O) ratio for line 1 of dataset 1, fitted using approach A. 85

Figure 34 - STEM-EELS data on the niobium oxide interface (a) Niobium oxide Nb:(Nb + O) EELS maps as a function of the etch time (b) Depth profiles derived from EELS spectra, taken from Altoé *et al*[27]. 86

Figure 35 - Image of the PANalytical EMPYREAN XRD machine. 101

Figure 36 - The optics settings and parameters used in the XRD measurements. 102

Figure 37 - The XRD signal from all five treated Niobium samples 103

Figure 38 - The XRD signal from all five treated Niobium samples (zoomed version) 104

Figure 39 - Magnified scale showing the peaks near 39 degrees 105

Figure 40 - Magnified scale showing the peaks near 56 degrees 105

Figure 41 – Peak for all samples 70 degrees 106

Figure 42 - (a) Secondary electron image from the Nb - Au interface and (b, c, d) EDX elemental maps of O, Au, and Nb respectively. 109

Acknowledgments

This thesis paper could not be written without the help and support of Prof. Arthur Blackburn, my supervisor, and Prof. Rogério de Sousa, my co-supervisor, who gave me support and assistance and provided motivation and encouragement throughout the entire period of my research thus far. My deepest gratitude goes also to my family and friends for their moral support. I also wish to thank all of my collaborators who helped me complete this thesis.

Dedication

To my parents,

To my brother, Poya

and to my friends.

Chapter 1: Introduction and Motivation for Research in Superconducting Niobium and Niobium Oxide (NbO_x)

1.1. Literature Review and Problem Statement

This section presents the physical foundations of superconductivity and applications and the relevance of niobium and niobium oxides (NbO_x) in the field of superconductivity.

1.1.1. Superconductivity Physics and Applications

Superconductivity refers to the property of certain materials to exhibit zero electrical resistance and complete diamagnetism when they are below a specific temperature [1]. This means that electricity can flow through these materials without any energy loss with a perfect ability to resist magnetic fields. The critical temperature is the temperature below which superconductivity appears and is often referred to as T_c. When a superconductor is cooled below its critical temperature (T_c), its resistance decreases suddenly to zero. [2][3]

Superconductivity has been a topic of intense research since its discovery over a century ago. This property holds great promise for many applications, including energy storage and power transmission, magnetic resonance imaging (MRI), particle accelerators, quantum computing hardware, and others. However, many of the materials that exhibit superconductivity have limitations, such as a low critical temperature (e.g.

9.25 K for niobium while room temperature is approximately 273 K) or high production costs, which hinder their practical use [1].

The superconductivity property that does not permit a magnetic flux density to exist inside the metal is referred to as the Meissner effect.[4] When an external field is imposed on a superconductor, it creates surface currents that cancel the external magnetic field within the material [5].

There are two categories of superconductors, known as type I and type II [6]. In type I superconductors, once the applied field reaches a certain critical value H_c, the Meissner state is completely lost and the material no longer exhibits superconductivity [5]. Type II superconductors have two critical fields, a lower one H_{c1} below which the material is in the Meissner state, and an upper one H_{c2}. Between the two critical fields, the superconductor enters what is known as the mixed or vortex state. In this state, the magnetic flux is present within the material in the form of a lattice of magnetic vortices. By increasing the magnetic field, more vortices enter the material [7].

1.1.2 Superconductivity in Niobium

Niobium is a material that has received a significant amount of attention due to its superconducting properties [8][9][10] such as high critical temperature compared to other superconductors, strong type-II superconductivity, high critical current density, low cost, and high availability [11].

Niobium has the highest critical temperature and the highest critical field H_{c1} of all the pure metals. T_c = 9.25 K for niobium which is quite high compared to other superconductors [11]. Thus, niobium can become superconducting at liquid Helium temperature (T = 4.15 K), which is relatively simple to access.

Niobium is a type-II superconductor, meaning that it can maintain its superconductivity in the presence of high magnetic fields. This makes niobium particularly attractive for high-field magnets and other applications that require a high magnetic field. For example, the superconducting niobium has been widely used as the preferred material for many applications, such as for the creation of accelerating cavities in particle accelerators [11] and the production of superconducting qubits, which are a key component of some quantum computers. Superconducting qubits are tiny circuits made of superconducting materials that can maintain a quantum state for a long time, which is necessary for carrying out quantum computations. One of the most common types of superconducting qubits is the transmon qubit, which is made using a niobium-based superconducting material. It is possible to produce large arrays of qubits on a single chip, which is necessary for building practical quantum computers. In addition to its use in qubits, niobium is also used in other superconducting components of quantum computers, such as read-out resonators [12]. Superconducting wires are capable of carrying an extremely high current (thousands of Amperes) through a relatively small wire, while experiencing little to no energy loss. This allows them to generate strong magnetic fields that are impossible to achieve using regular wires.

Superconducting niobium are being used in particle accelerators as superconducting cavities to increase the energy of particles. Niobium is a suitable material for constructing Superconducting Radio Frequency (SRF) cavities due to its short magnetic penetration depth (32 – 44 nm), the highest transition temperature ($T_c = 9.25\ K$), and its low resistance which results in high current carrying ability with low loss. The last feature makes niobium a good candidate in applications with high gigahertz (GHz) frequencies where the skin depth of a conductor becomes very small, and the power handling and high-field capabilities of the conductor become important. Also, niobium superconducting films are used in Superconducting Quantum Interference Devices (SQUIDs), which are magnetic field sensors with high sensitivity, utilized in applications such as medical imaging and quantum computers with tunable qubit frequencies. Figure 1 shows some of the important applications of niobium: as elements of a quantum computer (Figure 1(a)), and as a SRF cavity for particle accelerator (Figure 1(b)).

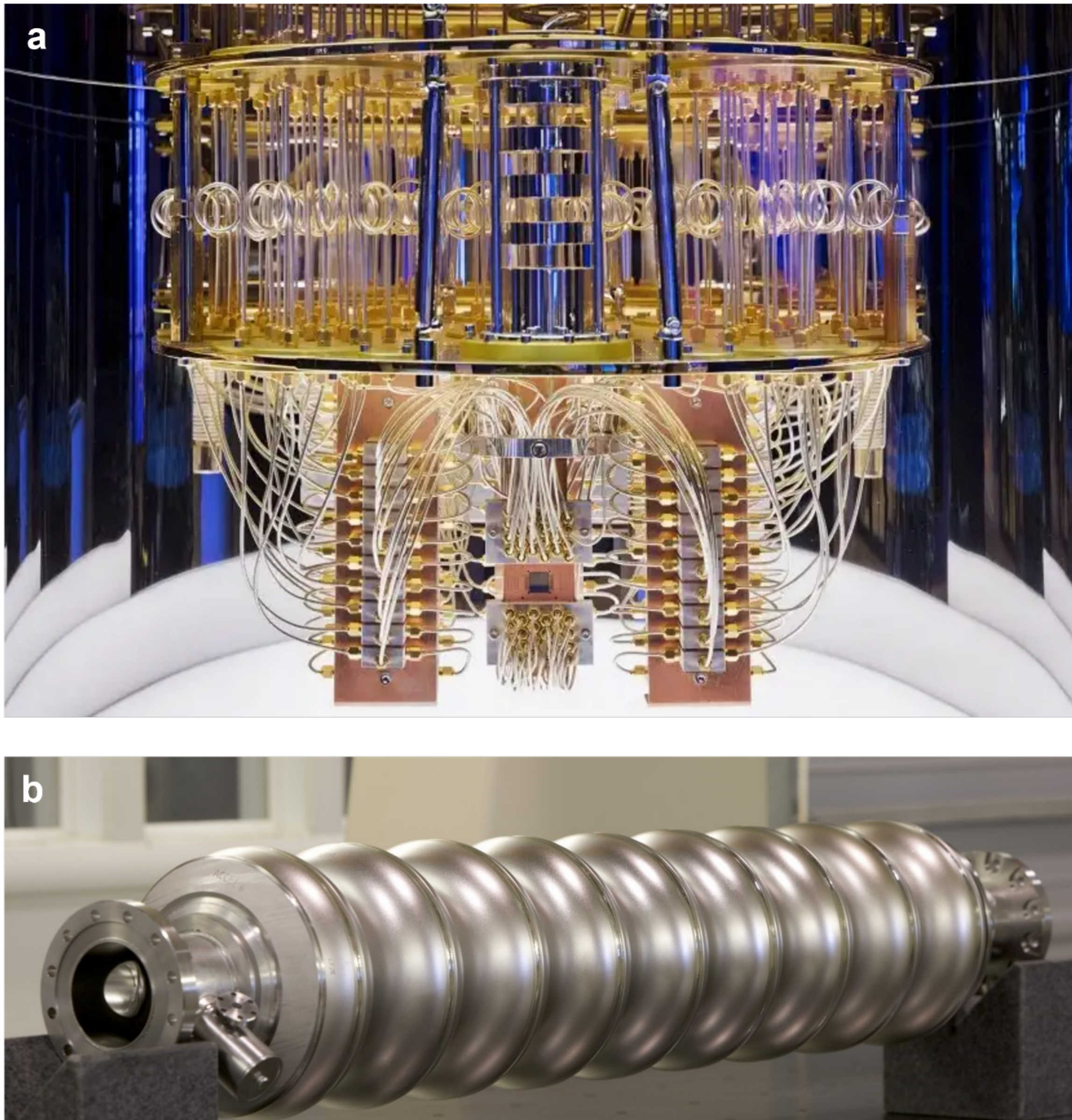

Figure 1 - (a) An IBM quantum computer, mounted on the plate of its fridge cooling system[1], and (b) an SRF accelerator cavity[2].

[1] https://ibm-research.medium.com/quantum-computing-and-ai-to-enable-our-sustainable-future-58aa494cd4bc
[2] https://td.fnal.gov/srf-department/

Besides niobium, niobium oxide (NbO_x) is a dielectric material with a wide range of applications, including use in electrical and electronic devices, catalysts, and abrasives. NbO_x is an important metal oxide, primarily because it limits the performance of Nb-based devices [13]. Dielectric losses limits the performance of SRF cavities and leads to energy relaxation/decoherence in Qubits [14].

1.1.3 Importance of Defects in Superconductive Niobium and Niobium Oxide

Defects in a material can have a significant impact on its physical, chemical, and electrical properties. In the case of niobium, defects such as impurities, vacancies, interstitials, dislocations, and grain boundaries can have a profound impact on the superconducting properties of the material [15][10]. The type and concentration of defects can affect the electrical conductivity of niobium and alter the critical temperature and critical field [16]. One approach to improving the superconductivity of niobium is to minimize defects through processes such as annealing and doping [17]. For example, studies have shown that annealing niobium in a controlled environment can improve its superconducting properties by reducing the microstrain in the material [18].

With regards to niobium oxide (NbO_x), defects can also affect its physical and chemical properties, and understanding these defects is important for optimizing the performance of niobium oxide-based materials. One type of defect commonly found in niobium oxide is the oxygen vacancy, which is a missing oxygen atom in the NbO_x lattice. These vacancy defects can change the electronic structure of the material,

introducing new energy states within the bandgap. These states can trap electrons or holes, and reduce the effective bandgap, which makes it easier for electrons to jump from the valence band to the conduction band. This reduces the energy barrier for electrical conduction, which makes the material a poorer insulator and more conductive. Oxygen vacancies can be created by doping niobium oxide with other elements, or by subjecting it to high temperatures or low oxygen partial pressures during synthesis [19]. Oxygen vacancies can affect the electrical conductivity of niobium oxide, making it more conductive. Another type of defect found in NbO_x is the interstitial oxygen atom, which is an oxygen atom that is inserted into the lattice between niobium atoms. Interstitial oxygen can affect the optical properties of niobium oxide, as well as its stability and reactivity. Other defects that have been identified in niobium oxide include structural defects, such as dislocations and grain boundaries, as well as impurities, such as trace elements that are introduced during synthesis or processing.

Several methods have been developed to study defects in niobium oxide, including x-ray diffraction (XRD) as well as electron microscopy and spectroscopy techniques such as Electron Energy Loss Spectroscopy (EELS). These methods can provide information on the concentration, distribution, and nature of defects in niobium oxide, which can help increase our understanding of how defects affect the properties of the material.

1.1.4 Dielectric Loss and Quality Factor in Superconducting Devices

Dielectric loss and quality factor are important parameters for understanding the behavior of devices constructed from niobium that are operated in the superconducting state [3][20][21][11].

Dielectric loss refers to the processes whereby electrical energy is absorbed by defects and quasiparticles that possess electrical polarization in the material. This energy is transformed into heat due to the coupling of the polarization degrees of freedom with phonons [15]. The amount of dielectric loss in a particular material is obtained by measuring the quality factor Q of an electrical resonator made of this material [14]. The quality factor for a resonator is defined as

$$Q = \frac{f_r}{\Delta f} \tag{1.1}$$

where f_r is the frequency of the resonance and Δf is the linewidth of the same resonance, with $\Delta f = 1/(2\pi\tau)$, arising from the finite lifetime τ for photons in the material.
In resonators made with normal (non-superconducting) metals, $1/\tau$ is dominated by Ohmic loss due to finite conductivity. In contrast, resonators made with superconductors have Ohmic loss drastically reduced because of the nearly infinite conductivity of the superconducting state. As a result, the Q-factor of superconducting resonators has been shown to be in the range of 10^5 to 10^7 for planar qubits such as the transmons made with thin film niobium wires, and up to 10^{12} for 3d resonators such as the TESLA cavity

made for particle accelerators. The extremely high Q for electrical resonators made with superconducting niobium make them suitable for a wide variety of high-precision applications such as qubits, particle accelerators, microwave filters, and oscillators.

Experiments in resonators and waveguides show that most of the energy loss in superconducting devices occurs at the surfaces and interfaces of the superconducting wires [22]. The microscopic origin of this loss has been identified to be two-level system defects with electric dipole moment. In TESLA cavities that contain only niobium and niobium oxide, the loss was shown to be exclusively due to a single two-level system (TLS) species with a sharp distribution of modulus of electric dipole moment [23]. A two-level system (TLS) refers to the presence of two closely spaced energy levels within the material's structure. These energy levels are usually associated with defects or impurities in the material. TLS appear to be present in the surface/interface dielectric layers of niobium, though their exact physical origins and locations are still not known. The work here aims to give some insight into their locations and physical structures.

The presence of TLS leads to losses in superconducting devices. These losses limit the performance of superconducting qubits, which are used in quantum computing, and other superconducting devices such as microwave resonators and detectors [24][25][23].

TLS loss is mainly generated at the interfaces between materials and in bulk dielectrics, which have a higher density of TLS compared to the bulk material. Thus, controlling the

TLS density at these regions is essential for reducing energy dissipation and maximizing Q-factor in Nb devices [23].

The energy dissipation due to dielectric loss is generally higher at higher frequencies. In niobium SRF cavities, the RF fields are typically in the range of hundreds of MHz to several GHz, and losses limit their ultimate performance since input power becomes converted to heat rather than being directed towards accelerating the particles in the cavity [26].

Reducing dielectric loss can be achieved through various approaches, such as reducing the surface roughness, and controlling the oxygen and other impurity content in the material [27].

1.1.5 Conclusion of the Literature Review about Defects in Superconductive Niobium and Niobium Oxide (NbO_x)

Niobium is a widely used material for applications that benefit from or require a superconducting state. Research on the role of defects in Nb and its associated native surface oxide continues to be an active area of investigation, because TLSs of unknown origin were shown to dominate dielectric loss and limit the value of the Q factor for resonators. The development of new techniques to better characterize the defects and microstructures at the Nb/Nb oxide surface/interface is an active research area. Efforts to reduce dielectric loss through surface passivation techniques are ongoing.

1.2. Research Motivation and Scope

While it is known that dielectric losses limit the performance of many important superconducting device applications, and experimental data has been fitted to give the loss mechanism as being partly attributable to transitions within a two-level system (TLS) model [14], the physical location and physical structure of the TLSs are not known. The aim of this study is to conduct a comprehensive examination of the surface oxide layer using electron microscopy and XRD to gain insights into the potential locations and origins of the TLSs.

Studies have shown that most of the energy relaxation is happening in the oxide surface of the niobium and two-level systems defects are responsible for this [28]. To expedite exploration of the location and origins of the TLS, we first need tools and techniques to characterise in more detail the current (likely oversimplified) pictures of the oxide layer. Usually the surface oxide is considered as a simple stack of amorphous Nb oxides, with a gradient in oxide concentration, that increases towards the surface [10]. The most stable polymorphs of NbO_x are NbO, NbO_2, and Nb_2O_5 [10], and these are generally considered to occur in sequence on the surface of Nb [29]. However, the Nb-O system is exceptionally complex system with a vast number of polymorphs and metastable states [10]. It is also known that even within so-called amorphous materials, there is short and medium range order that is influenced by material preparation conditions [30].

Several recent investigations [27][31] have focused on characterizing various forms of niobium oxide present in the NbO_x layer. Nevertheless, the techniques employed in these recent studies still provided only limited data regarding the structure of the surface oxide, with many remaining open questions and potential disagreements with prior studies. In this thesis, the aim is thus to scrutinize and extend existing high-resolution thin-film characterisation methods that have been used to date to characterize the NbO_x layer. Specifically, the focus is on high-resolution electron microscopy, with an emphasis on a novel method of EELS analysis that rapidly and with greater confidence produces useable oxide layer microstructural and thickness parameters. It is anticipated that these parameters could in due course be correlated with dielectric loss properties on a series of Nb devices, where the native oxide was formed under differing conditions. If correlations, or even no correlations, were then drawn between these parameters and losses, this would then be an important step to localizing the TLS origins within the surface oxide or interface between the oxide and niobium.

Chapter 2: Introduction to Electron Microscopy and Focused Ion Beam Instrumentation

This chapter provides a high-level overview of electron microscopy and Focused Ion Beam (FIB) instrumentation. These are the primary tools used to characterize and prepare sample materials in this dissertation.

2.1. Overview of Electron Microscopy

Electron microscopy is a technique used to observe the internal and surface structure and composition of materials, cells, and biological specimens and it is the only technique that can give sub-angstrom imaging [32][33]. This technique uses a beam of electrons instead of light to produce high-resolution images. Electron microscopy has revolutionized the field of materials science, biology, and medicine by providing detailed insights into the structures and functions of biological and non-biological systems.

There are two main types of electron microscopy: transmission electron microscopy (TEM) and scanning electron microscopy (SEM). In TEM, the electrons pass through the specimen, and the resulting image shows a projection of the internal structure of the specimen. SEM uses a focused beam of electrons to produce images of the surface of a specimen. With environmental SEM, it is also possible to investigate biological and other materials at atmospheric or low vacuum pressures, to gain views of the sample material in its native state [34].

Transmission electron microscopy (TEM) can achieve resolutions of a few tenths of a nanometer (0.1 nm or less) for imaging thin specimens. Scanning electron microscopes (SEM) can also achieve high resolution for imaging surfaces, with resolutions ranging down to a few Ángström, in the best cold field emission gun microscopes. In practice, the achievable resolution of an electron microscope is often limited by various factors, such as specimen preparation, electron beam stability, and detector noise. Therefore, the actual resolution achieved in practice can vary depending on the specific instrument and conditions used. [35]

There are also some limitations to TEM. For example, specimens must be thin enough to allow electrons to pass through them, and the samples must be carefully prepared and sometimes coated with a thin layer of metal or other conductor to allow charge deposited in the sample to be rapidly dissipated without introducing resolution impacting charge build up. Furthermore, electron microscopy can be time-consuming, requires specialized equipment and expertise, and is more expensive than other imaging techniques.

Overall, electron microscopy plays a crucial role in the fields of materials science, biology, and medicine. Some recent advances in electron microscopy include the development of cryo-electron microscopy, which enables scientists to study biological specimens in their native state while frozen in vitreous amorphous ice [36].

2.2. Overview of Focused Ion Beam (FIB)

Focused Ion Beam (FIB) is a powerful nanofabrication and characterization technique that uses a beam of ions to cut, mill, and deposit material. FIB, in combination with micro-manipulators, allows for precise manipulation of materials at the nanoscale, making it a valuable tool in fields such as material science, electronics, and biology [37][38].

FIB works by directing a focused beam of ions at a material, which then sputters away material. Control of the focused ion beam current, beam energy and the time spent on the sample allows for precise control over the area being milled and the depth of milling. This makes FIB ideal for creating and modifying nanoscale structures and for preparing samples for transmission electron microscopy.

In addition to milling, FIB can also be used to deposit material, such as metals or insulators, in precise locations by using ion-beam induced deposition from a gaseous precursor which is introduced in the system close to the area where the beam encounters the sample. This makes FIB a valuable tool for creating nanoscale electronic devices, such as transistors, and for repairing damaged devices.

FIB has several advantages over other nanofabrication and characterization techniques. For example, FIB allows for the creation of three-dimensional structures, unlike techniques like photolithography, which are limited to two-dimensional structures. FIB

also enables the creation of structures that are not possible with other techniques, such as those with steep walls or sharp corners.

However, FIB also has some limitations. For example, FIB is limited in terms of the speed of material removal, making it time-consuming and difficult to use for large-scale nanofabrication; one must also be wary of redeposition of material removed from the sample or workpiece in un-desirable directions away from the cutting face; and in general a small amount of the focussed ion beam material is embedded in the sample which may influence its surface properties.

Nonetheless, FIB plays a crucial role in the field of nanotechnology, providing a powerful tool for creating and manipulating nanoscale structures, having particular use in preparing samples for TEM inspection as discussed next.

2.3. Sample (Lamella) Preparation for Electron Microscopy using FIB

Lamella sample preparation with FIB is a technique used to create thin cross-sectional samples from a bulk material. As discussed earlier, for electron transparency, the thickness of the material/sample for characterization with TEM often needs to be less than 50 nm to make full used of aberration-corrected TEM instruments.

The process of preparing a lamella sample with FIB involves the following steps (also shown in Figure 2):

1. **Mounting the bulk material:** The bulk material is mounted onto a substrate, such as a silicon wafer, and then coated with a thin layer of metal, such as gold or platinum, to make it conductive.
2. **Focused Ion Beam Milling:** A focused beam of ions is directed at the bulk material in a specifically shaped pattern (as will be described in more detail in the next section) to produce thin cross-sectional slices of the material. The milling process can be controlled to create slices of the desired thickness, usually in the range of tens of nanometers to a few micrometers.
3. **Transferring the Lamella:** Once the slice has been milled and thinned appropriately, the lamella is transferred to a TEM grid or another substrate for further analysis.
4. **Characterization:** The lamella sample can then be characterized using transmission electron microscopy (TEM), scanning electron microscopy (SEM), or other techniques to study the internal structure and composition of the material.

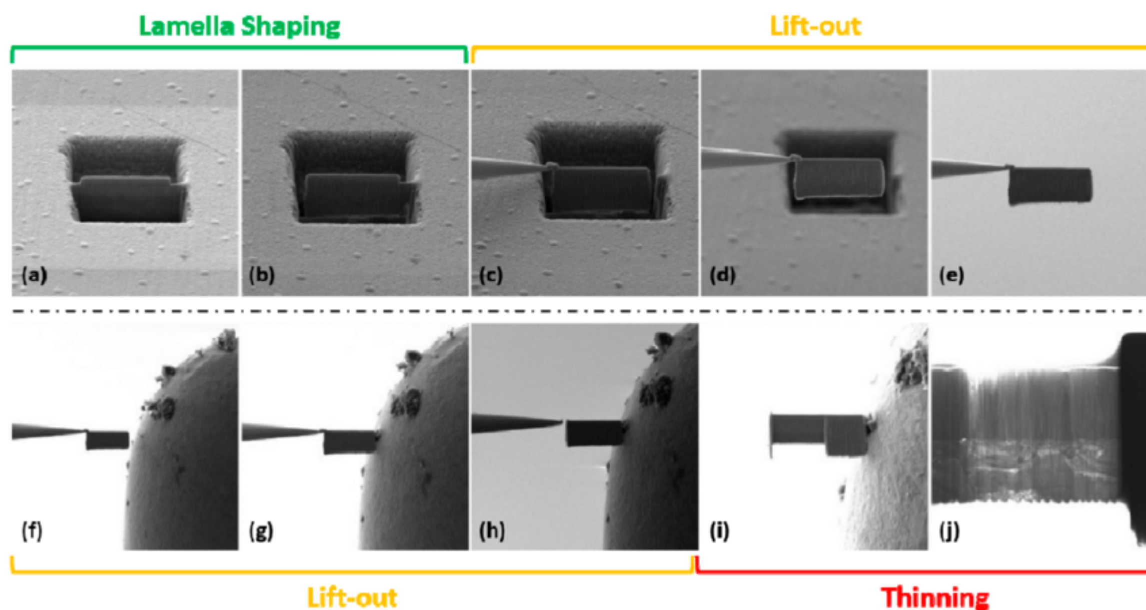

Figure 2- SEM images of the main steps regarding TEM lamella preparation: (a) FIB digging; (b) border cut; (c) nanomanipulator welding; (d–f) lamella displacement; (g) support welding; (h) nanomanipulator detachment; (i) thinning; (j) lamella analysis with STEM. (Figure taken from [39]**).**

The lamella preparation steps will be discussed in more detail in section 3.4.

2.4. Overview of Electron Energy Loss Spectroscopy

Electron Energy Loss Spectroscopy (EELS) is a powerful analytical technique used in materials science and electron microscopy to help determine the chemical composition of materials at high resolution, and in some situations gain insights into the electronic structure of material [40].

EELS works by analyzing the energy loss of electrons after they have passed through the sample material. When electrons collide with the atoms in a material sample, as

illustrated in Figure **3**, they can lose energy due to inelastic scattering, which results in the emission of characteristic spectral lines from optical to X-ray wavelengths. The X-ray spectral lines are related to the energies of the inner-shell electrons of the atoms in the material and can be used to determine the chemical composition of the material. The energy carried away by the X-ray photon comes from the primary electron beam which consequently loses energy in the interaction.

The resulting energy loss spectrum is measured by passing the emerging beam through and beam-bending magnetic spectrometer. This energy spectrum can be used to determine the elemental composition and electronic structure of the material, and to study the distribution of elements within the material.

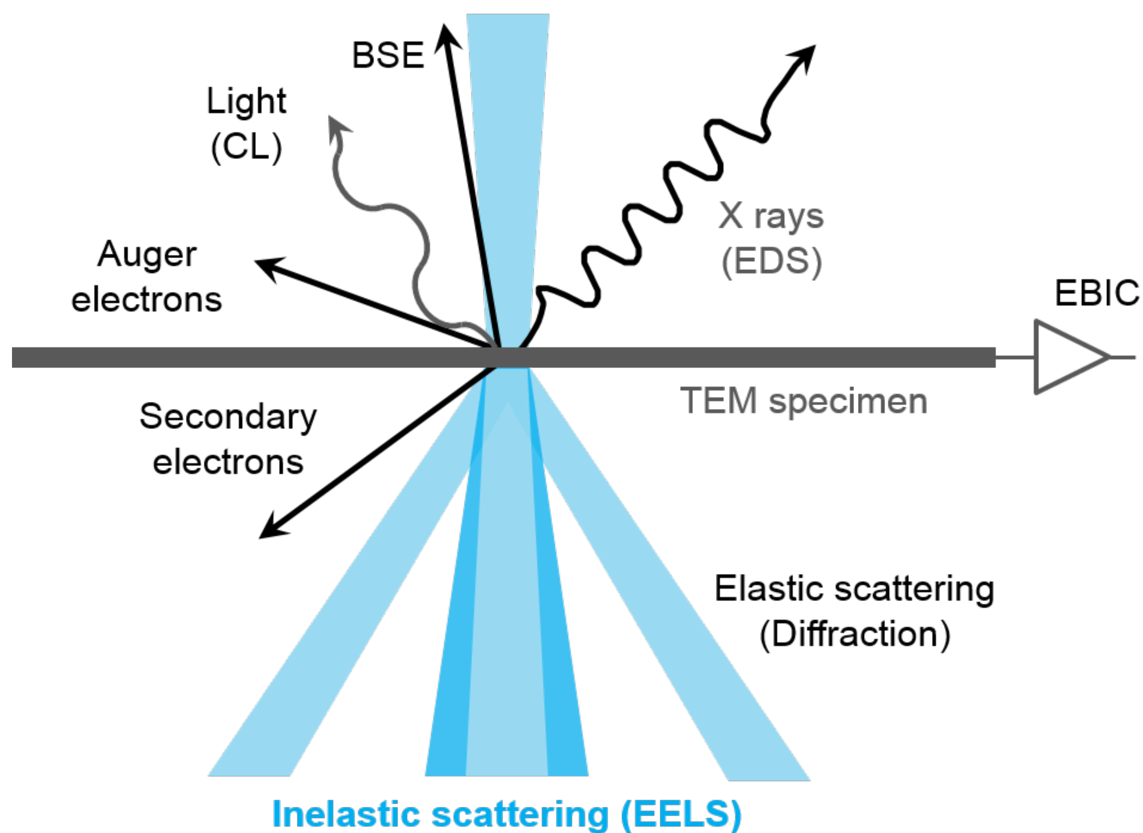

Figure 3 – **Illustration of the electron beam interaction with a sample in a TEM. The electron beam (blue) enters the sample from the upper side and transfers energy to the outgoing modes shown with outgoing arrows. The emerging beam thus has less energy than the incoming beam.** [3]

A typical EELS spectra is shown in Figure 4. In EELS analysis, the background and signal integration are important steps in the data processing and analysis. In the example of Figure 4, the spectrum must be decomposed into a background, integration of the

---

[3] https://www.gatan.com/techniques/eels

signal above this fitted background performed as a first step towards determining the elemental composition of the material.

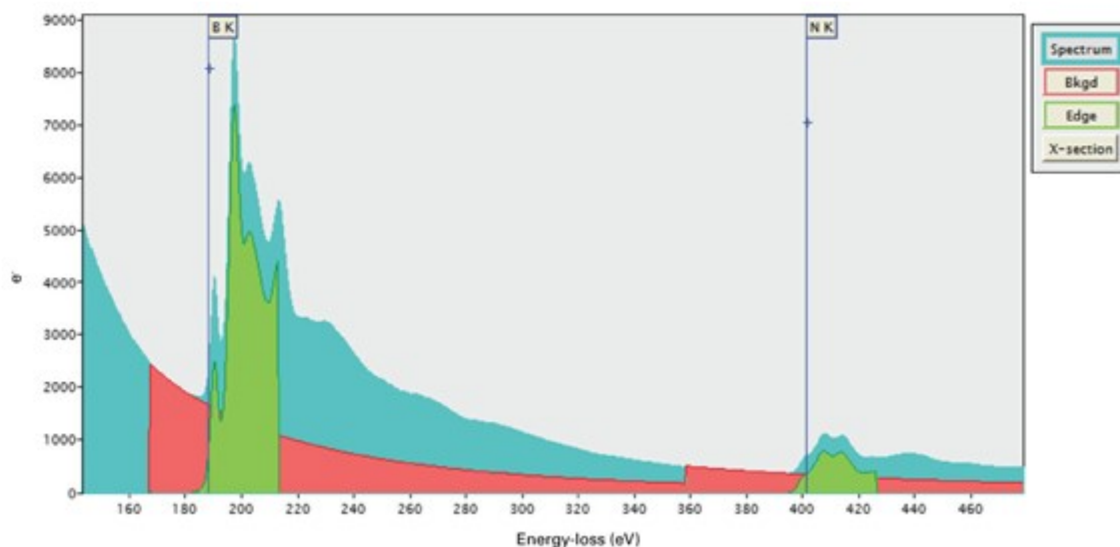

Figure 4 – A typical EELS spectra for boron nitride. The vertical axis, labelled e^-, gives the number of electron counts. [4]

By extrapolating the background signal fitted to the region prior to the onset of a particular ionization edge and subtracting this background from the region where the edge is expected, it is possible to obtain a quantitative estimate of the concentration of the corresponding element. This is illustrated in Figure 5.

[4] The example taken from https://eels.info/how/quantification/extract-signal

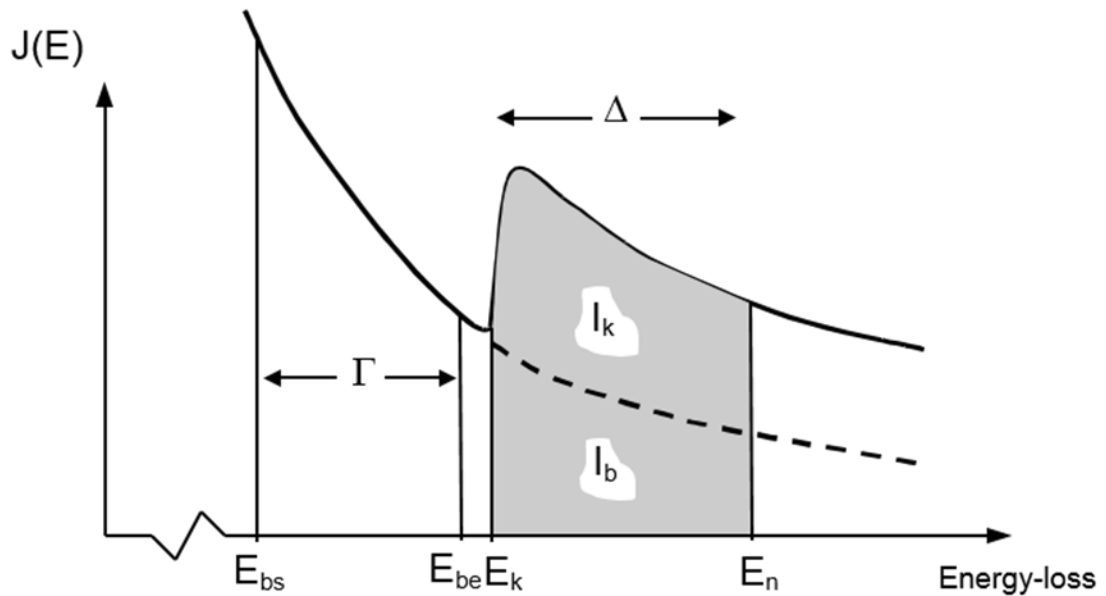

Figure 5 - Background fitting and signal integration regions on a typical EELS sharp onset core-loss edge. *Γ* = background fit window; Δ = signal integration window; I_b = background intensity; I_k = signal intensity.

The areal density, which is atoms per unit area, can be found with the following relationship.

$$N = \frac{I_k}{I_1 \sigma_k}, \tag{2.1}$$

where *N* is the areal density (atoms / nm^2), I_k is the sum of all counts in the edge (excluding background), I_1 represents the integral of the low-loss spectrum up to an energy loss Δ, and σ_k is the cross-section for ionization of an electron in the associated shell. [40]

The background signal in EELS primarily comes from losses or processes occurring at preceding lower energy edges, which overlaps with the signal or energy window of interest.. In addition to this, there can be underlying noise and fluctuations in the data that are not related to the elemental composition or previous edges. Example noise sources are detector noise (thermal and readout), sample and spectrometer electronic drift, and fluctuations in the electron beam energy and current. To obtain a high-quality EELS spectrum, it is important to accurately remove the background signal, which can be done using various techniques, such as polynomial fits, rolling averages, or filtering algorithms [41][40][42][43][44][45][46].

Signal integration in Gatan EELS involves calculating the area under the peak in the EELS spectrum to obtain the intensity of the signal. The area under the peak can be calculated using various techniques, such as Gaussian fits or other algorithms. The signal intensity can then be used to obtain information about the material, such as the atomic number, chemical composition, and bonding states.

The power law model is commonly used for background subtraction in EELS spectra. The power law model describes the background signal as a power law function. The power law background fit function is given by:

$$J(E) = A\,E^{-r} \,, \tag{2.2}$$

where J is the current (or current density) at the energy loss, E, and A is a scaling constant and r is the slope exponent.

In TEM instruments fitted with a Gatan energy filter, both background subtraction and signal integration are readily and typically performed using their proprietary software, specifically Gatan Digital Micrograph (sometimes also referred to as Gatan Microscopy Suite, GMS). This software provides a range of tools and algorithms for processing and analyzing EELS data, allowing for quick analysis of the sample properties. However, the relative apparent simplicity of applying this advanced analysis in this software can rapidly lead to erroneous results. As the manufacturer point out on their website (https://eels.info/how/quantification/extract-signal) there are many pitfalls and subjective judgements that are often taken in setting up integration windows and background models, which often do not follow the power background law given above and thus lead to erroneous signal levels and quantification. Niobium, having a broad onset edge, is particularly prone to some of these errors.

Chapter 3: Niobium and Niobium Oxide (NbO_x) Sample Preparation and Electron Microscopy Characterization

In this section, I present the steps that were taken to prepare the material samples used in this thesis. I explain the experimental steps from bulk sample preparation through to the details of FIB lamella preparation. Sample characterisation is explained starting with initial bulk sample characterization using X-ray Diffraction (XRD). XRD was performed to screen a set of samples we intended to look at in the TEM and perform EELS analysis on, to get an overview of bulk crystalline sizes, and perhaps see some weak diffraction signatures related to the surface oxide that had previously been overlooked. Finally, some electron microscopy details and results are presented, though discussion of the novel EELS analysis techniques developed is deferred until chapter 4.

3.1. Bulk Niobium Metal Source and Specifications

The niobium used in this thesis was purchased from ATI Wah Chang (based in Oregon, USA) which is a rare metals extraction facility. Their specification of the elemental composition of the samples are shown in Table 1 (in parts per millions - ppm) in 5 analyzed samples. The treatments for the samples are described in section 3.2.

Table 1 - Elemental composition of the samples. Concentrations are given in ppm and the table headings identify the samples, which are as described in section 3.2.

Element	BCP	1400C	120C	75+120C	N-infused
C	20	20	20	20	20
Fe	25	25	25	25	25
H	3	-	-	-	3
Hf	50	50	50	50	50
Mo	30	30	30	30	30
N	20	-	-	-	20
Ni	20	20	20	20	20
O	40	-	-	-	40
P	30	30	30	30	30
Si	25	25	25	25	25
Ta	190	230	170	150	170
Ti	30	35	31	31	30
W	30	30	30	30	30
Zr	50	50	50	50	50
Nb	Balance	Balance	Balance	Balance	Balance

A grain size test was performed following ASTM E112 test. ASTM E112 is a standard test method used to determine the average grain size of metallic materials. The test is commonly referred to as the "Standard Test Method for Determining Average Grain

Size". The ASTM E112 test method involves preparing a metal sample by grinding and polishing it to a flat surface. The surface is then etched with a solution that reveals the grain boundaries. The etched surface is then examined under an optical microscope, and the grain size is determined by measuring the diameter of individual grains and using a statistical formula to calculate the average grain size.

This test showed 20%-4.5 and 80%-6.5. The number "20%-4.5" means that 20% of the grains in the material are between 4 and 4.5 grains per square millimeter (or as specified in the test). Similarly, "80%-6.5" means that 80% of the grains in the material are between 6 and 6.5 grains per square millimeter.

3.2. Various Treatments on Bulk Niobium Samples

The bulk niobium samples used in this study were treated with five different methods. Five bulk niobium samples with 10 mm by 10 mm approximate dimensions were hand polished in order to remove the edges that were produced during machining and cutting. Next, a buffer chemical polishing (BCP) was then performed on each samples to remove the damaged surface layers. The sample with the name BCP had only these two steps. Then the four remaining samples were annealed for 5 h at 1400° C to remove pre-existing and machining-induced stress within the Nb followed by a final BCP (10 μm) to

eliminate any contamination possibly introduced from the oven. The sample with the name 1400C did not go through further processes. One of the three remaining samples was baked at 120°C for 48h; this sample is labeled as 120C. Another sample was baked at 75°C for 5 h followed by a 120°C bake for 48 h; this sample is labeled as 75+120C. The last sample was sent to FNAL (Fermi National Accelerator Laboratory) for nitrogen infusion, which involves heating the sample to 800°C under a vacuum for 3 hours, followed by gradual cooling of the sample to a temperature of 120°C under a flow of nitrogen in the furnace at a pressure of 25 mTorr. The sample was kept at this temperature and pressure for 48 hours [47]. This sample is referred to as N-infused [48]. An optical image of all the samples are shown in Figure 6.

Figure 6 – Optical images of the prepared bulk niobium samples, showing approximately half of the sample covered with a gold protection layer. The samples are all approximately 15 mm wide.

3.3. Characterizing Crystallinity and Grain Size of Treated Bulk Niobium Samples using X-Ray Diffraction (XRD)

Before picking a niobium sample for further microscopic and spectroscopic characterizations, X-Ray Diffraction (XRD) was used to characterize the crystallinity and grain size distributions of treated bulk niobium samples. A summary of the XRD results and analyses are presented in this section, and further details are provided in Appendix A.

The XRD signal from all five treated niobium samples are overlaid in Figure 7. These results show three predominant peaks at Bragg angles of 39, 56, and 70 degrees, which are associated with niobium's (011), (002), and (112) crystalline planes. The sharpness of the peaks is an indication of the crystallinity of the sample.

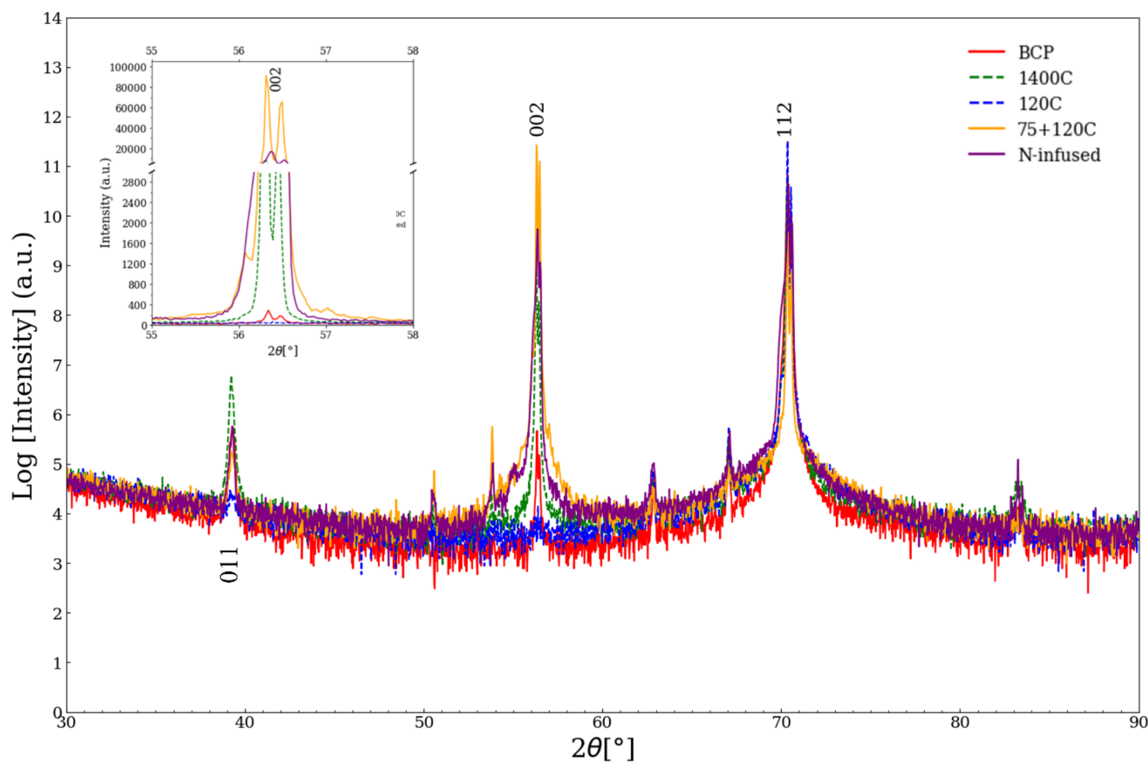

Figure 7 - XRD spectra of the samples used in this study, inset with an enlarged view of the 002 peak.

The XRD results were analyzed using the Scherrer method for grain size estimation described in Appendix A. The average crystallite size of the materials was calculated based on the two predominant peaks at 56° and 70° and presented in Table 2. Though we made no detailed considerations of the error in the extracted grain sizes, visible observations of the peaks in Figure 7, showed strong variations in widths. These widths in turn relate to grain sizes, and we thus felt that the trends in Table 2 were valid, without requiring detailed evaluations of errors in these measurements. For our purposes at this stage we were looking for trends rather than precise numerical values.

Table 2 - Average crystallite size of the samples based on the average grain size extracted from the three main XRD peaks (39°, 56°, and 70°).

Sample Name	BCP	1400C	120C	75+120C	N-infused
Average Crystallite Size [Microns]	0.6	0.4	1.9	2.5	1.3

3.4. Preparing a Lamella Sample using Focused Ion Beam (FIB)

Due to time limitations and the complexity of the subsequent lamella sample preparation and TEM characterization, only one sample (BCP) was chosen for a more detailed analysis, including TEM imaging, EDX spectroscopy, and Electron Energy Loss Spectroscopy (EELS). This section describes the lamella sample preparation method in detail.

The Lamella sample cutting and preparation process for EELS measurements was first performed with a Hitachi FB-2100 Gallium ion beam machine at the University of Victoria. However, this machine is a single-beam system, which means that the ion beam is utilized to perform the sample cutting at polishing (at high-intensity), and the same ion beam is used at lower intensities to create an image to enable the operator to interact with the sample. As a result, the use of an ion beam for creating a contrast can cause damage to the sample. Also the Lamella sample prepared with this machine can only be thinned to a certain limit, which may not be sufficient for creating a sample that is transparent to

200 keV electrons used in this TEM. Ideally the aim is to have a sample thickness at or below 40 – 50 nm.

Therefore, the final sample was made using a dual beam system, which contains a Scanning Electron Microscope (SEM) coupled with a Ga Focused Ion Beam (FIB). The machine used for creating the final sample was a Helios SEM/FIB at the Electron Imaging and Holography Facility at the Simon Fraser University (SFU).

The following sections describe the steps taken in preparing the Lamella samples for the subsequent microscopy and spectroscopy purposes.

3.4.1. Depositing a Protective Gold Layer on Bulk Nb Samples using Physical Vapor Deposition (PVD)

As described earlier, the motivation of this research is to study the NbO_x layer at the interface of niobium. However, this layer is prone to damage caused by exposure to the focused ion beam used in Lamella sample preparation. As such, prior to using the dual-beam SEM-FIB system to cut the Lamella sample, it is essential to deposit a protective layer on top of the material to prevent the surface from being damaged by the focused ion beam, and to keep the Nb / NbO_x interface at the surface of the material as intact as possible.

Moreover, in a FIB, the sample surface needs to be highly conductive to allow the electrical charge from electrons and ions to dissipate. This is because charged particles (electrons or ions) are exposed to the sample during the FIB process, and if the sample is

not conductive, this can result in a highly charged area on the sample which would deflect the electron or ion beam. In more details, the electrons or ions are collected by the sample and form a thin layer of electron depletion around the impact site. This layer of depletion prevents ions from penetrating the sample, which would result in undesirable charging and straggling effects. A conductive sample surface allows the electrons to flow away from the impact site, reducing charging and improving the beam stability. Therefore, a protective and conductive layer that does not oxidize is essential in this process, to ensure FIB Lamella preparation is possible, so that the NbO_x remains intact, and subsequent EELS measurements are not impacted. It is worth emphasizing that the envisioned EELS measurements are sensitive to any oxygen in the analysis area, so any foreign oxygen (such as from contamination) in the region can influence the result of the measurement.

To achieve these objectives, gold was chosen as the most appropriate protective layer. To keep part of the samples uncoated for other tests, half of the samples were covered by tape and 100 nm of gold was coated on the other half of the samples. Physical Vapor Deposition (PVD) was used to coat the gold protection layer on the samples. PVD is a sample preparation technique that involves depositing thin films of material onto a substrate surface by physical processes such as evaporation or sputtering. PVD produces high-quality, uniform thin films with precise control over thickness and composition.

3.4.2. Sample Preparation with Hitachi FB-2100

The Focused Ion Beam machine in the Advanced Microscope Facility at UVic was initially used for preparing the Lamella sample. This Ga ion beam machine is the Hitachi FB-2100, shown in Figure 8, which is operated with an accelerating voltage between 10 to 40 keV.

Figure 8 - Hitachi FB-2100 Gallium focused ion beam machine in the Advanced Microscope Facilities at the University of Victoria.

Sample BCP (see table 2) was the first candidate for lamella preparation. In order to prevent damaging to the part that was not coated with gold, the area was covered with Aluminium foil. Then the sample was put on the sample stage mounted with a clip and then put it into the machine.

To align the beam, an area is needed to be sacrificed. The surface of the sample was

quite even so any area could be used for the alignment. An area near the corner was chosen for this purpose since finding the corners is easier and we can keep the middle region unirradiated (intact) for creating the lamella. A 40 kV beam, constrained with a 80 μm condenser aperture, was used to initially align the beam. After aligning the beam, a region was chosen to cut out the lamella. Then a layer of tungsten was deposited on top of the gold for additional protection. The deposition was done with a same beam condition as for the alignment. The surrounding materials were removed by etching four rectangles with larger beam current surrounding the tungsten layer. The sample was tilted by 60° and the beam was then used to cut underneath the sample. At this point, the lamella is connected to the bulk sample with just a junction from one side and it is prone to failure due to breaking of the junction. The next step is lift-out. The sample was tilted to 20° and then the mechanical probe inside the FIB was positioned and welded to the probe to the side of the sample. Finally, the junction was removed. Figure 9 shows the steps from cutting surrounding materials to lift-out, and Table 3 below gives the lens and aperture settings for the various steps.

Table 3 – FIB beam settings used for the steps of lamella preparation. Lower condenser lens setting and larger aperture sizes produce greater beam current.

Step	Condenser Lens Setting	Aperture Size (μm)
Alignment	0	80
Deposition	0	80
Initial Cut	0	520
Undercut	1	300

Welding	0	80
Junction Removal	1	300

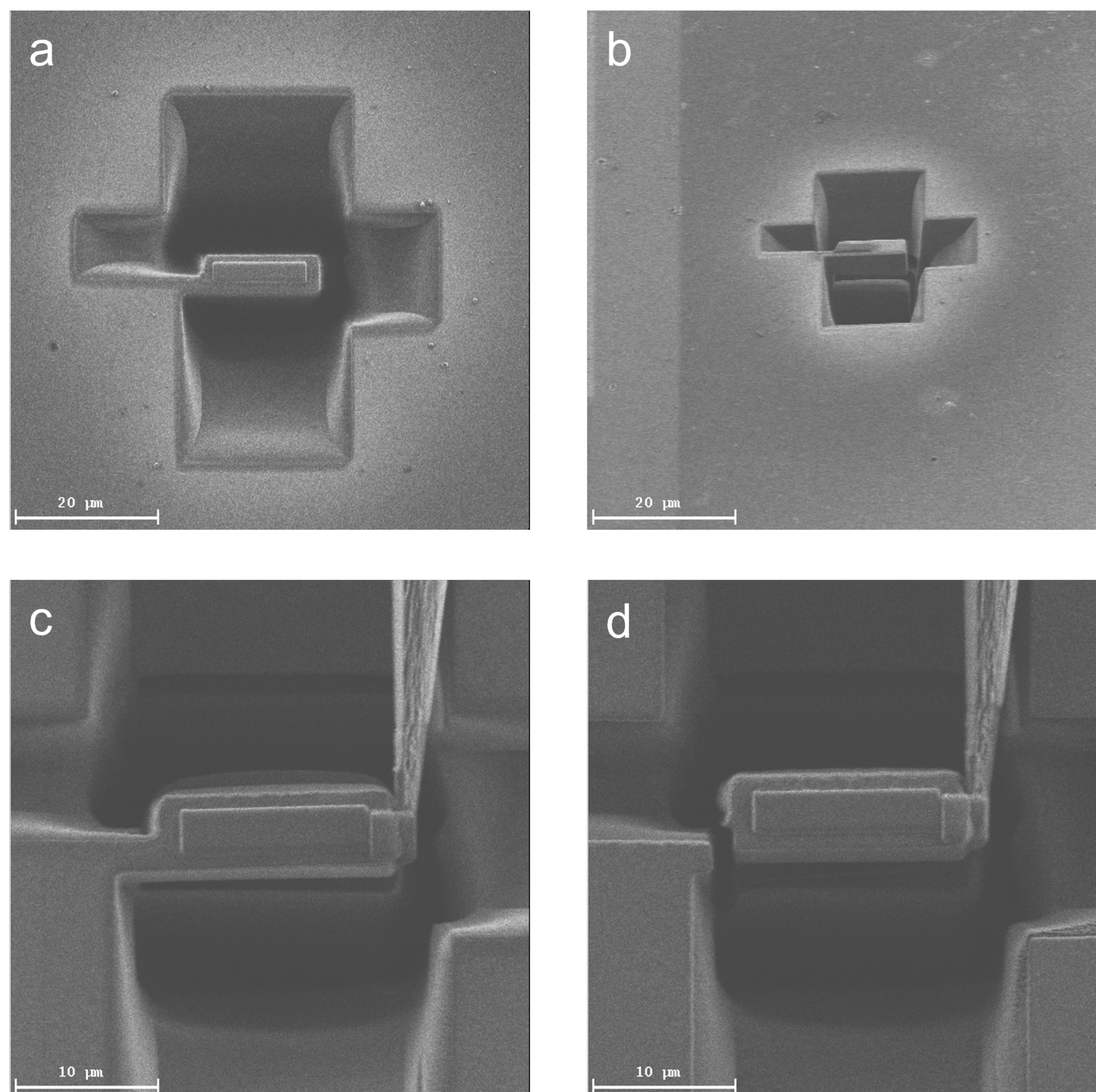

Figure 9 – Lamella preparation steps: (a) removing surrounding material; (b) lamella undercut; (c) attaching the lamella to the probe; and (d) removing the connection to bulk sample.

After lamella lift-out, the bulk sample was extracted from the machine, and a TEM half grid was loaded into the FIB. Figure 10 is a picture of 5 post Cu TEM half grid.

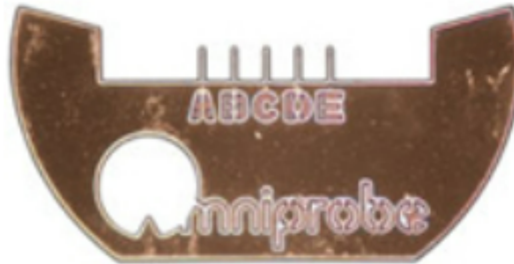

Figure 10 – Optical micrograph of a 5 post Cu TEM half grid (field of view and grid width is 3 mm).

One of the grid teeth was flattened and prepared for welding. Figure 11(a) shows a SEM image of flattened grid tooth and Figure 11(b – d) shows the lamella welded to the grid. Then the probe attachment was removed by using a relatively high-current 40 kV beam (using condenser lens setting 0, and an aperture size of 520 μm).

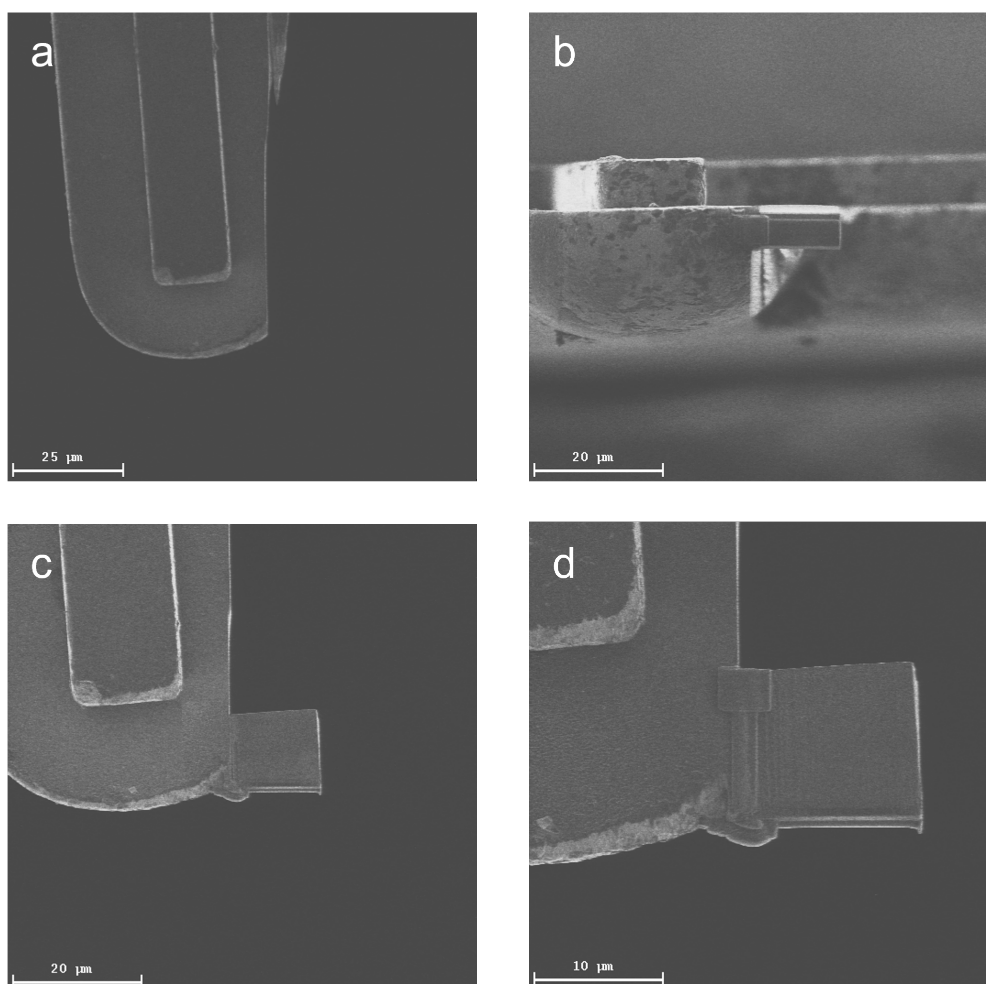

Figure 11 – SEM images of (a) flattened lift-out grid tooth, ready for welding, and (b - d) the lamella when welded to the grid, looking down the tooth (b) and from the side in (c, d). The scale bar units are µm.

Electron transparency of the lamella is necessary for EELS. For thinning, the same FIB machine was used instead of ion milling to polish the sample. The lamella was tilted and beam 30-1-15 (beam with the voltage of 30 kV and condenser lens and the aperture size of 15 µm) was used to polish the tip of the sample. Figure 12 shows the thinning process of the lamella.

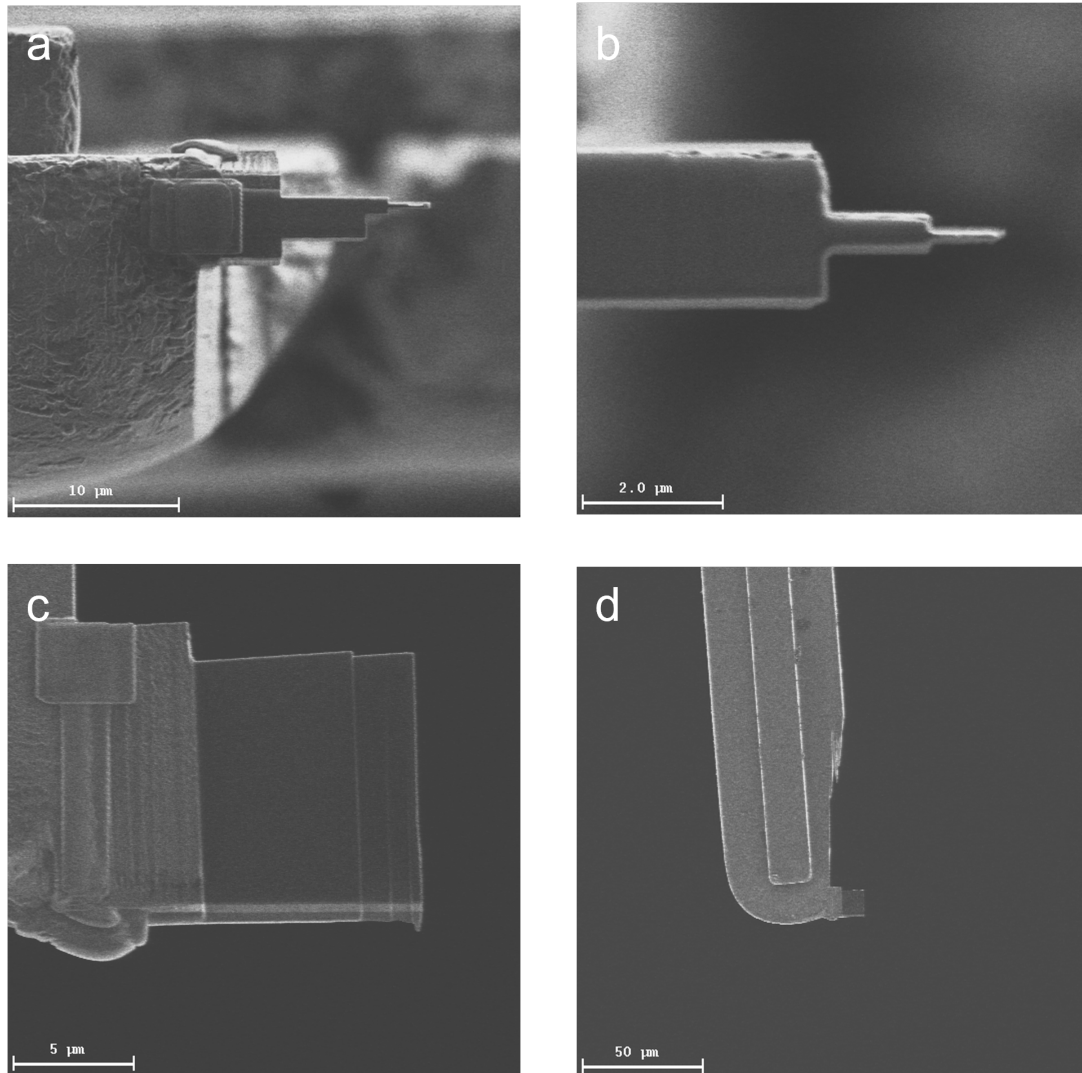

Figure 12 - FIB images of the final polished lamella taken with the lowest possible ion beam current in the instrument. Views are (a, b) from above and the side (c, d), where (b) and (c) give enlarged views.

3.4.3. Sample Preparation with Helios SEM/FIB

Upon examination of the prepared lamella under a scanning electron microscope (SEM), it was determined that the sample did not meet the required thinness criteria of 50 nm for

electron transparency. It was found that the use of the Hitachi FB-2100 machine caused damage to the sample, even during observation. Additionally, given that the sample was being prepared for EELS analysis, it was necessary for it to be uniform in thickness. Therefore, a dual beam focused ion beam machine (FEI Helios) was used to get to 50 nm thickness and surface quality. A dual beam FIB machine has one electron beam to image the sample and an ion beam for cutting and welding.

The final sample was made with this machine. An additional ion-beam induced deposition of platinum was deposited on the sample to further protect the gold coated niobium oxide layer on the surface of the niobium prior to cutting with the FIB.

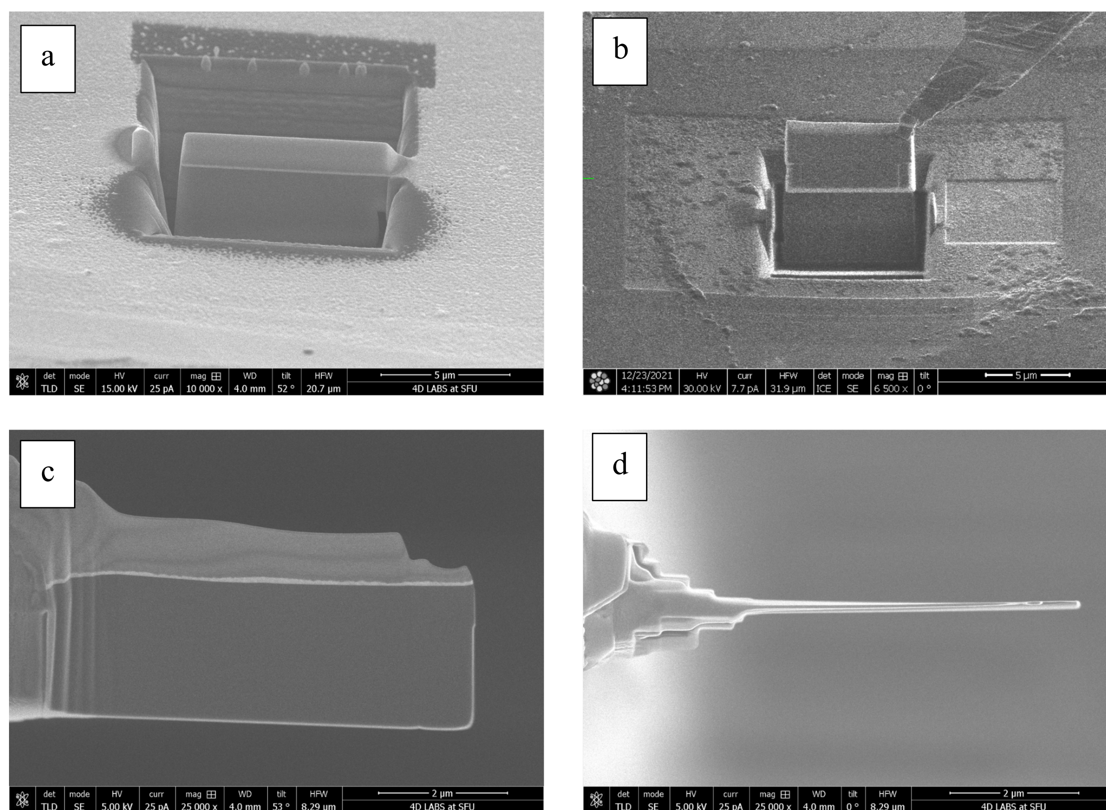

Figure 13 – SEM images of (a) the lamella cut, (b) lamella lift-out, (c) side view of final lamella and (d) top view of final lamella.

Figure 13 shows secondary electron images of the lamella preparation and lift out process along with images of final lamella.

3.5. Electron Microscopy Imaging and Spectroscopy on Lamella Sample

To ensure the suitability of the lamella sample for EELS analysis, various imaging techniques and tests were conducted to assess its uniformity and identify any inconsistencies. These evaluations aimed to obtain reliable and accurate EELS data by confirming the suitability of the sample for analysis.

A summary of the energy dispersive x-ray spectroscopy (EDX) results is presented in Appendix B.

3.5.1. Transmission Electron Microscopy of Lamella Sample

A Hitachi HF-3300V scanning transmission electron holography microscope (STEHM) was used for imaging the sample and carrying out EELS in this study. This machine has dual aberration correctors for operating in both TEM and STEM modes, and operates with beam voltages of 60 keV, 200 keV, and 300 keV.

Before commencing any measurement and analysis on the sample, it is necessary to obtain a preliminary understanding of the overall structure of the material in the sample. To achieve this, the sample was initially examined using bright field (BF)-TEM imaging at 200 keV. Figure 14 presents two BF-TEM images taken from the sample that shows the overall structure of the stacked layers of Nb and NbO_x and Au.

These images were taken with no objective aperture, and so the resolution was limited only by the envelope function bounding microscopes contrast transfer function and the tuning of the aberration corrector. The corrector was tuned to have phase surface flat to within $\pi/4$ radians out to 20 mrad here. Also prior to taking these images the sample was oriented while observing the diffraction pattern, to align a major crystalline zone axis to the beam direction. This procedure aimed to place the Nb upper surface as close as possible to parallel to the electron beam direction. We noted that the Nb region to the left of these images was a single grain with uniform crystalline orientation, as seen from

observing the diffraction pattern over a range of positions. As also expected from the XRD study the grain sizes were > ~500 nm in size. Thus, contrast seen within the Nb layer was attributed to surface texture and thickness variations due to FIB processing. Also, as noted later this Nb surface would re-oxidize after FIB processing, and so we may also be seeing thickness variations and underlying lattice - stress related effects from the re-oxidation of the exposed Nb here. These TEM images also revealed the NbO_x layer thickness is in the range of 4 to 5 nm, and to be nominally amorphous in nature. We will later compare this to EELS model analysis.

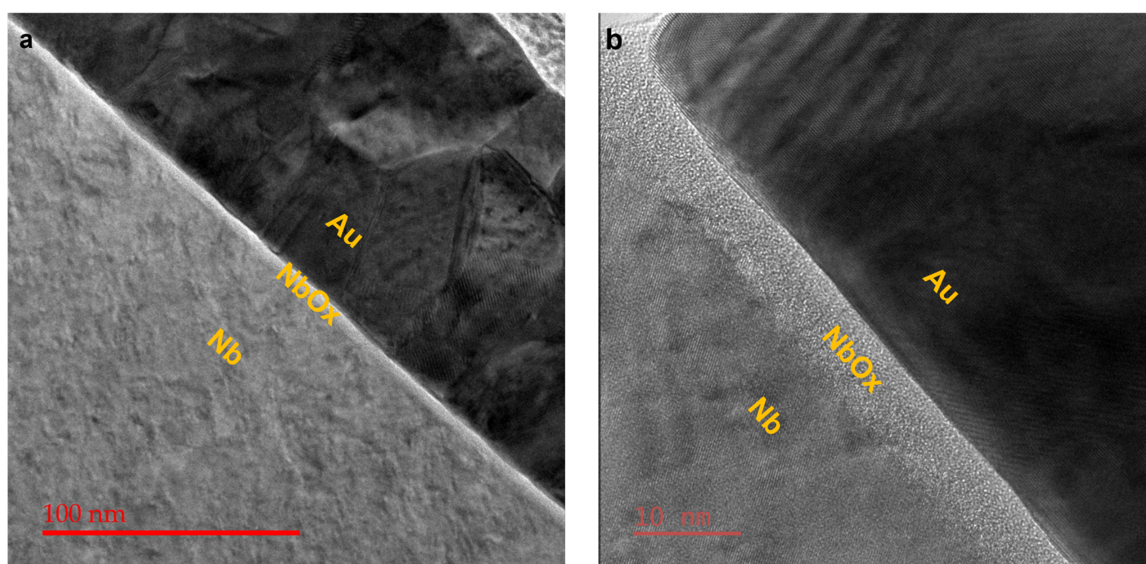

Figure 14 – BF-TEM images (200 kV) of the Nb, Au interface (a) magnification of 95 k (b) magnification of 410 k.

In the next chapter, the results of the EELS study is presented, along with a comprehensive analysis and modeling approach.

Chapter 4: Electron Energy-Loss Spectroscopy (EELS) Results and Analysis

This chapter describes the Electron Energy-Loss Spectroscopy (EELS) results and analysis for the niobium and NbO_x Lamella sample that was discussed in the previous chapter. It also proposes a new method of EELS analysis to determine the oxygen and niobium distribution in the surface oxide layer of the BCP sample. The next section describes the reasons why we feel an alternative method of EELS analysis is needed.

4.1. Introduction

As previously noted, the dielectric layer at the surface of superconducting materials is a critical region for energy dissipation and loss since this is where the TLS defects responsible for dielectric loss are located. To better understand the properties and structure of this layer, this chapter presents a novel method of electron energy loss spectroscopy (EELS) data analysis that gives parameters that describe the material composition in the NbO_x layer. This method provides valuable insights into the extent of the various types of oxides (niobium monoxide (NbO), niobium dioxide (NbO_2), and niobium pentoxide (Nb_2O_5) that are considered to be present in the dielectric layer.

The present investigation involved the examination of one sample of Nb (referred to as BCP) utilizing a novel EELS data analysis technique. Although this study is limited to a single sample, it is expected that this technique will be implemented for other Nb samples

prepared under diverse conditions in the future. It is anticipated that differing preparation conditions for the niobium may lead to subtle changes in the oxide layers, that in turn correlate to losses in devices made from these materials. Also, currently no direct imaging or EELS evidence of the structures that give rise to the TLS are known to exist in the surface oxide layer. The purpose of this study was to adopt a comprehensive and model-based approach to analyze STEM EELS data for improved comprehension of the oxide layer's composition. The study aimed to derive parameters from the EELS signal, facilitating reliable comparisons among a range of samples, including those measured on different electron microscopes. This information is of utmost importance for improving the quality factor of superconducting resonators.

Obtaining qualitative knowledge about the components of unfamiliar compounds and determining the location of elements within materials is a relatively uncomplicated process using EELS for elemental identification. However, generating accurate *quantitative* and precise compositional maps has always been an arduous and error-prone task [40]. This difficulty partly results from the methodology employed for extracting elemental data from EELS spectra.

It is important to note that EELS possesses both advantages and disadvantages. The strong advantage is its exceptional spatial resolution that exceeds that of energy dispersive X-ray spectroscopy (EDX) for example, and any other microbeam techniques. It is also particularly good at detecting low-atomic number elements, compared to say EDX. The disadvantage is that signals tend to be quite weak, and usually are present

above a non-linear background, where we have many offset peaks stacked on top of each other. Thus, just fitting peaks can be challenging. Even with a correctly fitted peak, extracting a quantitative measure of the material relies on an accurate predetermination of electron scattering cross sections. Thus, EELS has the disadvantage that obtaining quantitative information on an absolute or relative scale for materials/elements is very challenging.

While it could be argued that similar challenges exist for EDX techniques, background fitting challenges in EDX (or wavelength dispersive X-ray spectroscopy, WDX), have been better addressed as compared to EELS, in large part due to a much larger user-base and commercial impact of EDX. Despite EDX being lower resolution it is thus much easier and cheaper to implement.

The challenges that EELS presents for quantitative analysis are discussed next. In some cases, the background of the pre-edge region (see chapter 2) of a particular element is actually the tail of the peak from another element. This can make it difficult to obtain a good signal related to an element of interest, especially when the tail does not precisely follow the generally (but not always) theoretically expected power law form. In this situation, using a power law curve fit with an imperfect model for the background can cause false readings for an element.

Additionally, determining the areal density of the elemental species from measured EELS data necessitates using theoretically calculated scattering cross-sections or experimentally

determined cross-sections from a well-prepared sample. Theoretical and experimental cross-section measurements must consider the beam energy, convergence angle, collection angle, and possibly multiple scattering, which depends on sample thickness. Observationally, looking at many EELS composition maps presented in the literature, including those for example presented in this recent study [27], it would appear that often mapping data is presented without performing careful calibrations on similar or related known samples. It is perhaps an unfortunate situation and reality that researchers may occasionally present data from software bundled with electron microscopes without making detailed considerations of its validity.

To get around this issue, the method that is proposed in this study does not rely on careful calibration, and uses data produced from standard electron microscopy software, but processes it further to make it more robust against experimental issues and provide more meaningful parameters that this 'standard' software (specifically Gatan Digital Micrography Software, from Gatan Inc., Pleasanton, CA, USA). Also, it is important to note that actual EELS measurements involve samples with considerable thickness and contamination, which is often overlooked in other studies. Eliminating organic contamination, which often is present on samples in the electron microscope, is challenging during the long exposures necessary for EELS measurements though is crucial if standard analysis techniques are to be used. This contamination typically includes oxygen, likely from incorporated water or other oxygen containing organics, that can modify oxide maps. Moreover, the sample's significant thickness imply that the

microscope is sampling a relatively large conical volume with a Gaussian beam, rather than the ideal small cylindrical volume. Consequently, the detailed information within the sample is smeared out, or convolved with some Gaussian-like function, leading to some loss of resolution without some method of deconvolution.

Given that comprehending the structure of the oxide layer is vital for understanding possible loss mechanisms, the goal is to enhance the analysis of EELS data obtained from the oxide layer.

4.2. EELS Signal Model

Previous studies have demonstrated that the surface oxidation layer of niobium exhibits a layered structure, starting with NbO, followed by NbO_2, and finally Nb_2O_5 from the niobium surface [29], as illustrated in Figure 15. This picture has been gained from X-ray photo electron spectroscopy (XPS) studies [27], in combination with EELS. Getting meaningful data from XPS requires quite detailed model fitting, which has been performed [27], but detailed model fitting on EELS mapping data has not yet been performed; this is the goal of the current thesis.

Figure 15 shows that the total niobium oxide layer thickness t_3 is typically around 5 nm, as can be readily measured from regular high-resolution (HR-)TEM, as was shown in Figure 14. Elemental oxide thicknesses t_1 and t_2 are around 1 nm, but these cannot be observed directly in HR-TEM, as the oxide layer appears to be amorphous with no obvious delineations between the oxide layers direct imaging techniques. Also, there is

variation in the literature on the precise values of t_1 and t_2, and it would appear that they can vary to some extent depending on details of the material preparation conditions, such as the exposure time to air and/or process temperatures [49]. Also, it is currently unknown exactly how unform t_1 and t_2 are over the lateral extent of the surface. Some recent studies show the presence of nanocrystallite regions in the NbO_x layer, which in turn suggests that the layers are not entirely uniform in thickness [31].

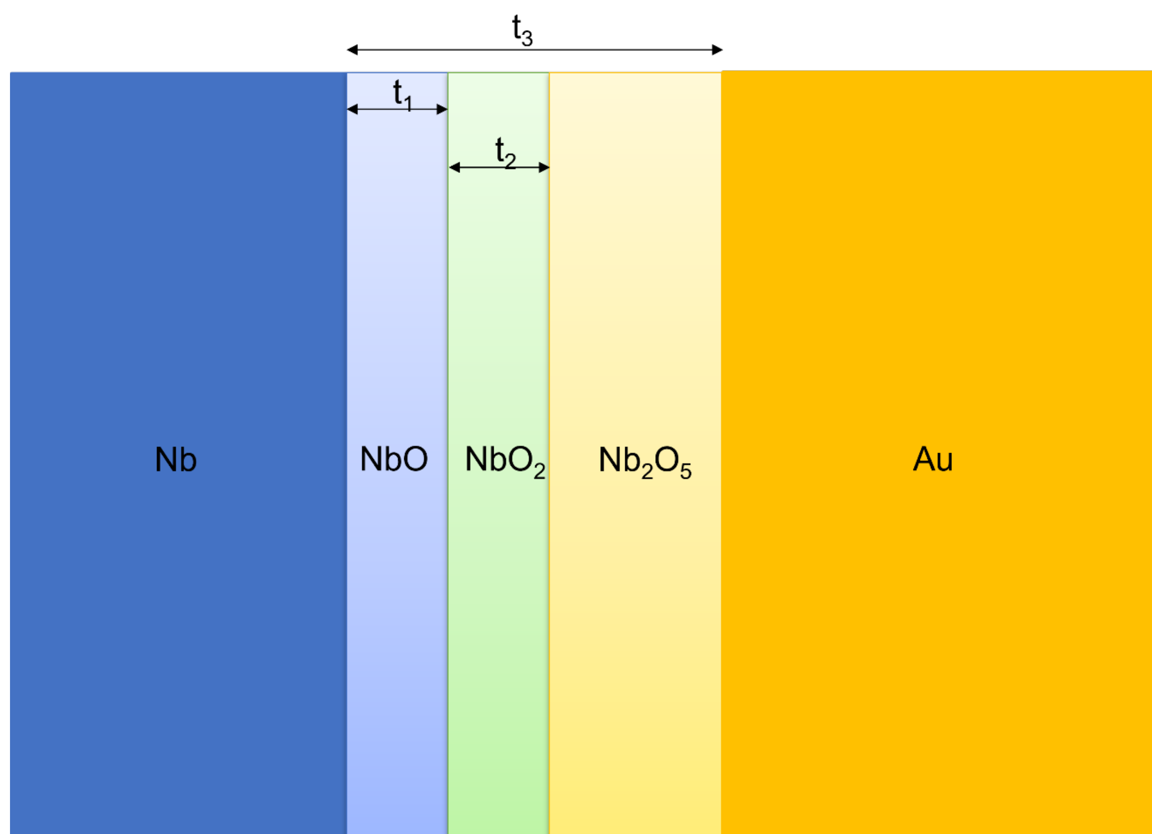

Figure 15 - Schematic of the layered structure of the NbO_x interface.

On the basis of the picture of the oxide shown in Figure 15, the relative concentrations and volume densities of Nb and O (with units of atoms/unit volume) would be expected to vary in a stepwise manner. This model is referred as ‘stepped model’. From the volume density the expected areal densities, measured in number of atoms (i.e. scattering centres) per unit area, can be determined by assuming a constant thickness in each region. The resulting characteristics for oxygen and niobium areal density, are shown in Figure 16(a).

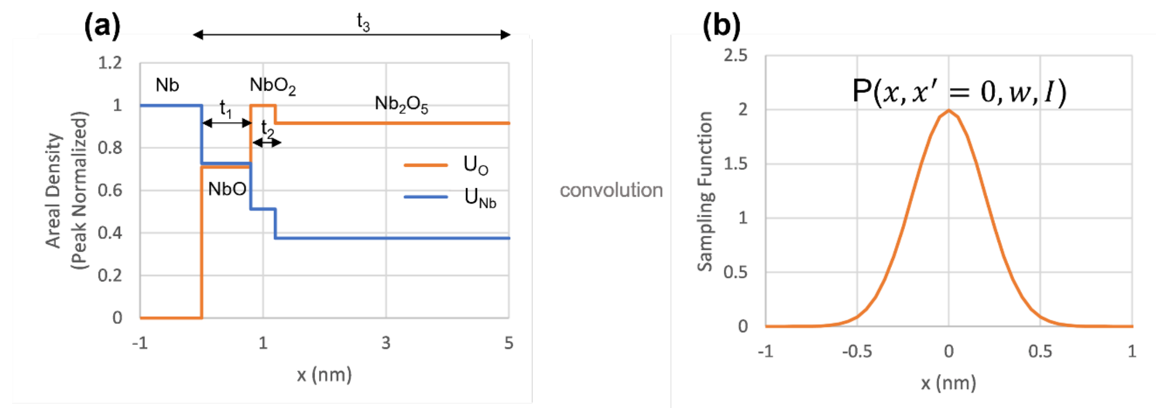

Figure 16 - (a) The underlying model of the areal density for approach A and (b) an example Gaussian that is convolved with the underlying model.

In Figure 16(a), the areal densities are given normalized to the local peak areal density that is observed. In this plot U_O is the peak normalized oxygen areal density, U_{Nb} is the peak normalized Nb areal density, and x is the distance through the structure (also shown in Figure 15). These values are determined from standard known values for the mass density for each of the oxide types, and simple atomic mass calculations. The relevant quantities are given in Table 4. The number of molecules per unit volume is simply

determined using $N = N_A \rho/M$, where N is the number of atoms/molecules in a specific volume, N_A is Avogadro's number, ρ is the density, and M is the molecular/atomic mass.

Table 4 – Volumetric density and peak normalized areal densities of Nb and O in the layers of our model. Peak normalization divides areal density by its maximal value. For Nb this is in the pure Nb layer, and for O this is in the NbO_2 layer.

Molecule /Atom	Number of molecules per cubic nm	Normalized Areal Density of Nb	Normalized Areal Density of Oxygen	Mass Density (g/cm^3)
Nb	55.6	1 (= η_1)	0 (= Ω_1)	8.6
NbO	40.4	0.73 (= η_2)	0.71 (= Ω_2)	7.3
NbO_2	28.4	0.51 (= η_3)	1 (= Ω_3)	5.9
Nb_2O_5	10.4	0.37 (= η_4)	0.91 (= Ω_4)	4.6

However, the stepped model depicted in Figure 16 assumes perfectly flat uniform interfaces between the different niobium oxide types. In reality though, real interfaces generally have some roughness and the focussed electron probe, which will ultimately probe this oxide layer, has a finite size and is approximately conical in form. To account

for the finite electron probe size and interface roughness, a Gaussian model point spread function (PSF) is introduced.

The selection of the Gaussian PSF is motivated by previous studies and research in the field [50], where it is common to consider an electron beam as having a Gaussian probe profile. This model has been widely adopted due to its simplicity, ability to provide a good approximation to the actual PSF, and widespread use. The PSF is described in Equation 4.1 and is also shown in Figure 16(b).

$$P(x,x',w,I)=\frac{I}{w\sqrt{2\pi}}\exp\left(-\frac{(x-x')^2}{2w^2}\right), \tag{4.1}$$

where x is (again) the distance through the barrier, x' is the centre position of the PSF, w is a parameter to describe the width of the PSF, and I is the intensity of the PSF, such that $I=\int_{-\infty}^{\infty}Pdx$. Note that w is related to the full width at half maximum (FWHM) of the PSF through $FWHM=2\sqrt{2\ln(2)}w\approx 2.355w$.

The final expected signal of a particular species would then be found through a convolution of the PSF with what is called the underlying model for the areal density, which could be U_{Nb}, or U_0 (as previously defined and shown in Figure 16), or U_{elem} for some element in general. The convolution represents the passage of the beam over the

oxide layer. The resulting signal from an element, S_{elem}, when the electron beam is at position x is then found through

$$\begin{aligned} S_{elem}(x) &= \int_{-\infty}^{\infty} U_{elem}(x') P(x,x',I_{elem},w)dx' \\ &= \frac{I_{elem}}{w\sqrt{2\pi}} \int_{-\infty}^{\infty} U_{elem}(x') \exp\left(-\frac{(x-x')^2}{2w^2}\right) dx' \end{aligned} \quad (4.2)$$

U_{elem} is assumed to be a function of position only, but is defined by other parameters such as t_1, t_2, and t_3 as thickness parameters, which will be discussed later. Going forward we introduce a shorthand notation for the above convolution that allows us to present the parameters only. The shorthand, given below, makes x an implied variable in the signal, and hides the integration:

$$\begin{aligned} S_{elem}(x) &= \int_{-\infty}^{\infty} U_{elem}(x',...) P(x,x',I_{elem},w)dx' \\ &\quad \textit{becomes} \\ S_{elem} &= U(...) \otimes P(I_{elem},w) \end{aligned} \quad (4.3)$$

Thus, when the $\otimes$ operator is used, the integration over x' is assumed to be taken, so that only the x dependence remains. The above ellipsis (…) is used to indicate the various parameters that define the shape (or form) of the underlying function, e.g. t_1, t_2, and t_3.

So far the model of the oxide is relatively simple, as depicted in Figure 15, but now shown again in Figure 18(a), this time with the additional protection layers and a schematic illustration of the electron beam passing through the sample.

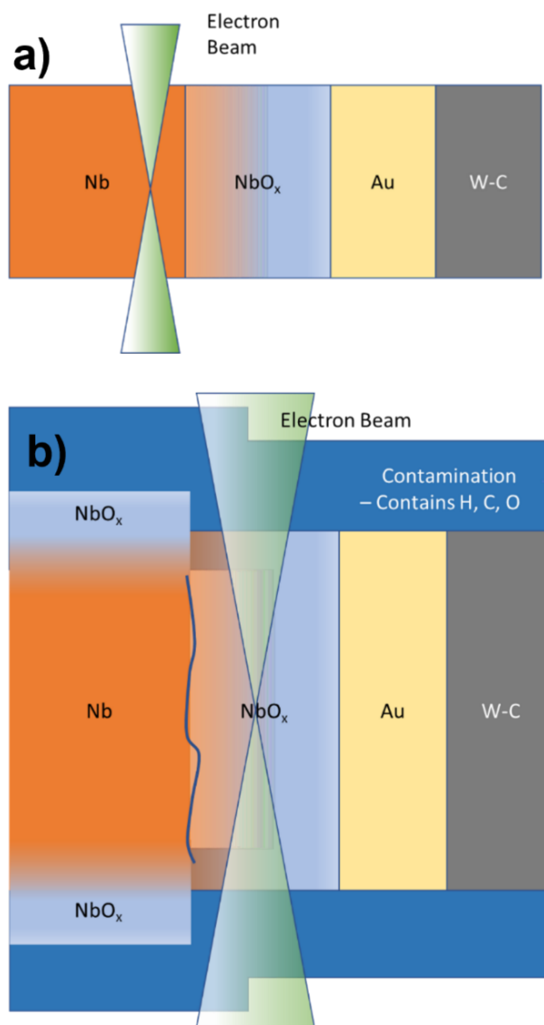

Figure 17 - Schematic illustrations of the cross-sections of (a) idealized lamella (b) actual lamella with an oxide layer on niobium part and contamination.

A more detailed and realistic situation is presented in Figure 18(b). Here, account is made for the fact that it is not possible to have a surface of niobium that is free of oxide. Unless the sample is transferred in some special vacuum transfer arrangement between the FIB and STEM, a native oxide will form on the freshly cut surfaces of the niobium. There is also an inevitable surface layer of contamination that forms on the sample in the electron microscope or focussed ion beam instrument, or arises from organics present in the air, unless extreme measures are made to keep the sample and microscope scrupulously clean. This is also depicted in Figure 17(b).

For the oxygen signal, the surface oxidation leads to an additional oxygen signal coming from the niobium before even encountering the oxide region of interest. This additional signal is denoted as a_O. There will also be an oxygen signal arising from the surface contamination. This background oxygen contamination signal is denoted as b_O and assumed to be constant over the EELS sampled area. It is worth noting that although Figure 16 depicts the oxide layer beginning at $x = 0$, it is unknown precisely where the oxide layer starts or ends during experimental data analysis. To address this uncertainty, a start position parameter x_s is introduced. Consequently, the complete model for the normalized areal density functions is as follows:

$$U_O = \frac{b_0 + \begin{cases} a_0 + \Omega_1 & x < x_s \\ \Omega_2 & x_s \le x < (x_s + t_1) \\ \Omega_3 & (x_s + t_1) \le x < (x_s + t_1 + t_2) \\ \Omega_4 & (x_s + t_1 + t_2) \le x < (x_s + t_3) \\ 0 & (x_s + t_3) \le x \end{cases}}{\max(\Omega_1, \Omega_2, \Omega_3, \Omega_4) + a_0 + b_0}, \quad (4.4)$$

$$U_{Nb} = \frac{b_{Nb} + \begin{cases} \eta_1 & x < x_s \\ \eta_2 & x_s \le x < (x_s + t_1) \\ \eta_3 & (x_s + t_1) \le x < (x_s + t_1 + t_2) \\ \eta_4 & (x_s + t_1 + t_2) \le x < (x_s + t_3) \\ 0 & (x_s + t_3) \le x \end{cases}}{\max(\eta_1, \eta_1, \eta_1, \eta_1) + b_{Nb}} \quad (4.5)$$

where η_{1-4} and Ω_{1-4} are defined in Table 4. Note that for U_{Nb}, a background parameter b_{Nb} is included. We anticipate a non-uniform layer of Nb over the sample (not shown in Figure 18). The additional background signal of niobium comes from the imperfect fit of a power law curve to the pre-edge region before onset of the edge related to Nb. A similar imperfect fit may also account for some of the background signal in oxygen, but more usually this is dominated by surface contamination of molecules containing oxygen.

An alternative approach to modeling the oxide layer is to consider the expected O:Nb areal density ratio, rather than looking at individual concentrations. This approach is referred to approach 'B' henceforth. Although it is feasible to derive this from the ratio of

the two aforementioned functions, it is practical to introduce a function for this ratio model, formulated as follows:

$$U_{O:Nb} = b_{O:Nb} + \begin{cases} a_{O:Nb} & x < x_s \\ R_1 & x_s \le x < (x_s + t_1) \\ R_2 & (x_s + t_1) \le x < (x_s + t_1 + t_2) \\ R_3 & (x_s + t_1 + t_2) \le x < (x_s + t_3) \\ 0 & (x_s + t_3) \le x \end{cases} , \tag{4.6}$$

where R_1, R_2 and R_3 are the stoichiometric ratios in the NbO, NbO_2 and Nb_2O_5 regions equal to 1, 2, and 2.5 respectively. Equation (4.6) reveals something interesting in the region $(x_s + t_3) \le x$ as the sample (without contamination) has no Nb or O in this region, the ratio between the two elements is 0/0. Numerically this is undefined, but here a value of zero is assigned as the model includes a background layer of O containing contamination shown in Figure 17. It is also interesting to note that if the sample was perfect with no contamination and we looked at the apparent O:Nb ratio in this region, we would expect to see a spurious signal related to the noise and other systematic errors in the EELS apparatus. An example $U_{O:Nb}$ function is shown in Figure 18, for the case where $a_{Nb:O} = b_{Nb:O} = 0$.

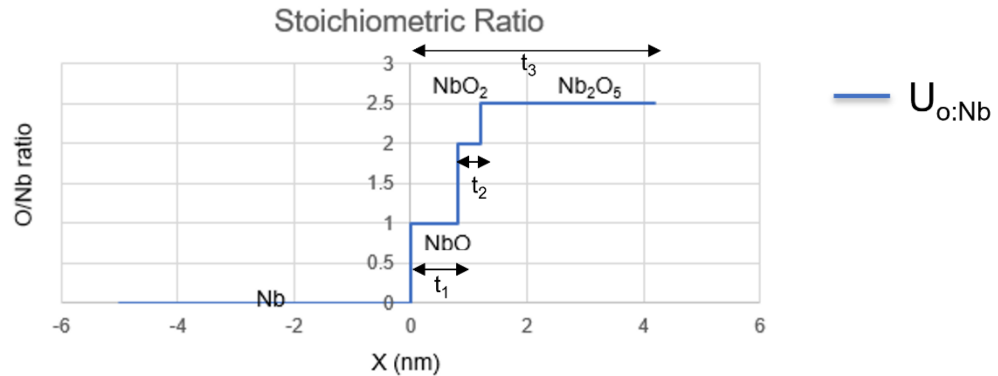

Figure 18 - Underlying model of the stochiometric ratio used in approach B.

In summary, the models can thus be described as below, using the notation given in Equation 4.3. The parameters in these models, though also described above are summarised in Table 5.

Nb-model: $U_{Nb}(x_s, t_1, t_2, t_3, b_{Nb}) \otimes P(w, I_{Nb})$

O-model: $U_O(x_s, t_1, t_2, t_3, a_O, b_O) \otimes P(w, I_O)$ (4.7)

O:Nb-model: $U_{O:Nb}(x_s, t_1, t_2, t_3, a_{O:Nb}, b_{O:Nb}) \otimes P(w, I_{O:Nb})$

After obtaining experimental data, the task of adjusting the parameters to minimize a measure of error between the model and experiment is then required. This is discussed after a summary of the experimental data collection in the following section.

Table 5 - Model parameters

Parameter	Description
I_{Nb}	Intensity of the niobium signal
I_O	Intensity of oxygen signal
t_1	Thickness of NbO
t_2	Thickness of NbO_2
t_3	Total thickness of the surface oxide layer
x_s	Starting position of the oxide on the line
$b_{Ox;}$ $b_{Nb;}$ $b_{Nb:O}$	Global background ('zero offset') to the oxygen, niobium or ratio signal accounting for EELS set up error, and/or the oxygen areal density
$a_{O;}$ $a_{Nb:O}$	Background added to the region to the left of the oxide in the figures, to reflect the fact that Nb will be oxidized on upper and lower surfaces before being placed in the TEM.

w	Width parameter of the PSF function

4.3. EELS Results and Data Processing

This section describes the procedures followed for data acquisition and preparation to facilitate subsequent analysis.

4.3.1. Electron Energy Loss Spectroscopy (EELS) of Lamella Sample

In order to obtain accurate results from the electron energy loss spectroscopy (EELS) measurement, it was necessary to carefully align the microscope. The instrument used was a Hitachi HF-3300V dual aberration-corrected electron microscope fitted with a Gatan 693 Quantum GIF EELS system. This was used in STEM mode at a chosen accelerating voltage of 200 kV, using 18 mrad beam half angle to produce a sub-1 Å focussed probe size. A focussed probe of this size is still considered state-of-the-art, despite some advances in aberration correctors in recent years. This is particularly helpful for EELS measurements, where the aim is to have the best possible spatial resolution.

In this study, two EELS measurement datasets were collected, referred to as dataset 1 and dataset 2. Table 7 presents key parameters of these datasets, and Figure 19 shows the regions surveyed overlaid on annular dark field (ADF) STEM images of the regions.

Table 6 - Measurement parameters for dataset 1 and 2

Dataset	Pixels	Step Size (nm)	Pixel Exposure Time (s)	Energy Dispersion (eV/channel)
Dataset 1	20 x 9	3.1	4	0.5
Dataset 2	38 x 7	1.4	4	0.25

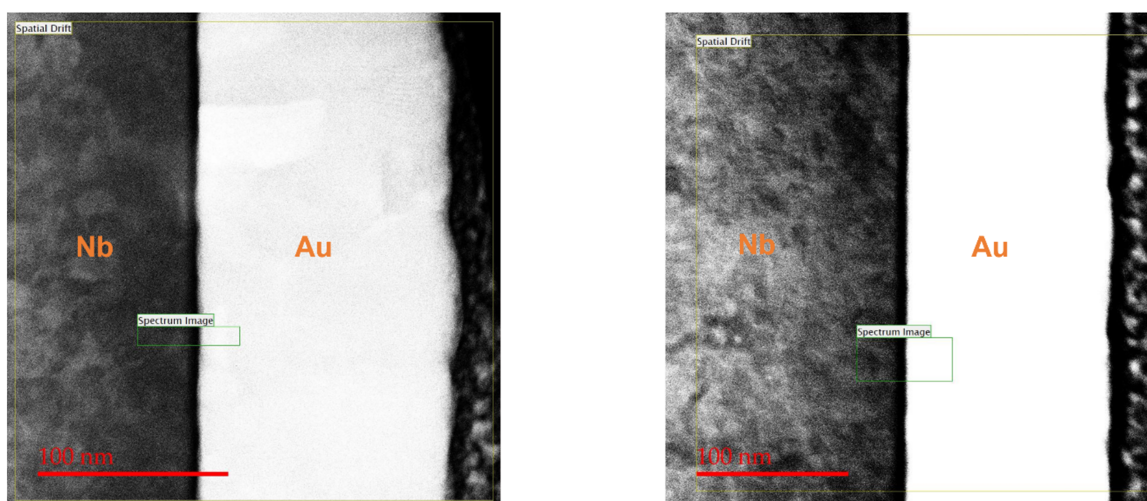

Figure 19 - Overview of survey regions (ADF STEM images) for dataset 1 (left) and dataset 2 (right). The regions surveyed are highlighted by the green rectangles.

Dataset 1 was a low-resolution dataset used primarily for initial testing of the data acquisition process, and dataset 2 was a higher-resolution set used for more detailed study. Note, however, that even in the high-resolution set (2), the step size was large compared to the focussed beam size of the instrument. This was intentional in order to achieve a compromise between total acquisition time, and sample drift. Note that the effective resolution of EELS in thicker samples is actually significantly greater than the

focussed probe size, as will be discussed in later sections. That said, had later accidental sample damage not precluded further sample investigation, it would have been desirable to acquire and analyze EELS data at higher resolution.

In electron energy loss spectroscopy (EELS) spectra, the Nb M edge is observed at 205 eV and the O K edge is observed at 532 eV. Both edges can be clearly seen in the datasets analyzed in this study. To obtain meaningful information from the data, it was necessary to remove the background and integrate the signal for each element. The background was removed by selecting a window just prior to the edge where no other edges were present, as described in Chapter 2. The background region is also shown shaded red in Figure 20 and Figure 21, for dataset 1 and 2 respectively.

The ratio of oxygen to niobium is a key factor in this study, and to obtain the most accurate quantitative ratio, equal signal integration windows were used for both elements. As shown in Figure 20 and Figure 21, the signal integration windows were set to 50 eV for dataset 1 and 20 eV for dataset 2.

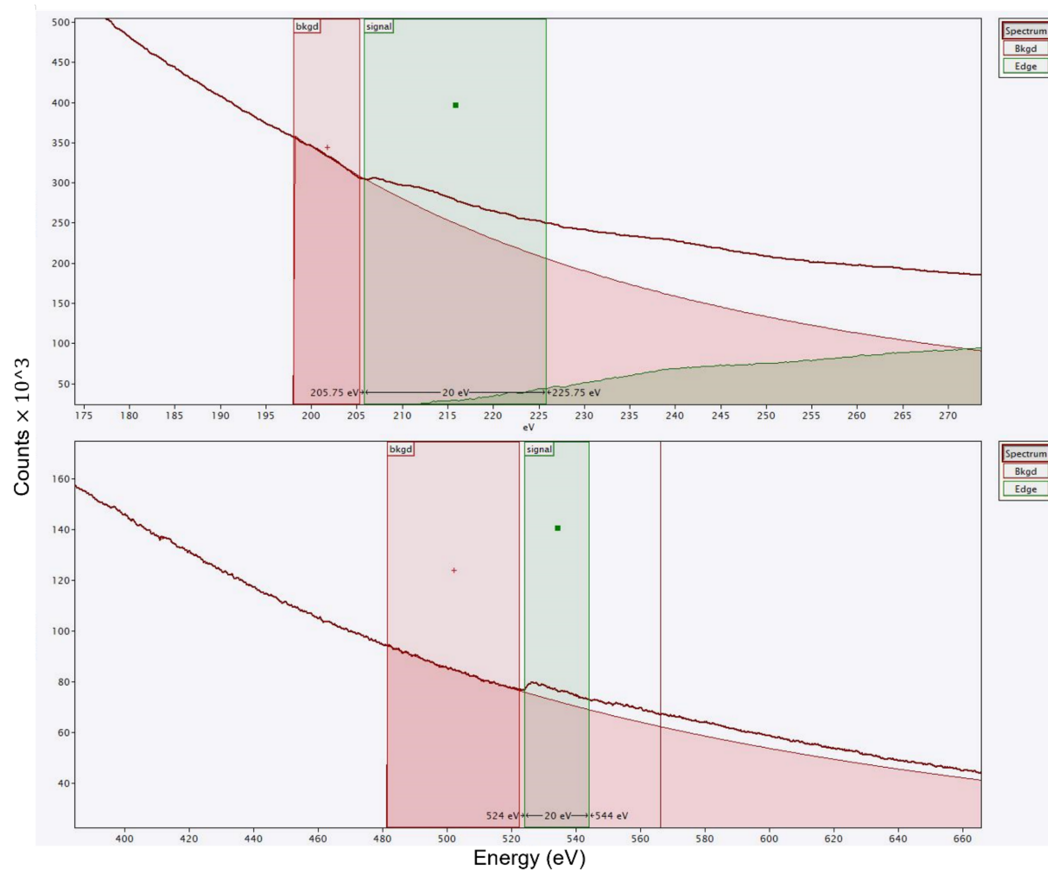

Figure 20 - Signal and background window for dataset 1. The upper panel shows the Nb edge on top and the lower panel shows the oxygen edge.

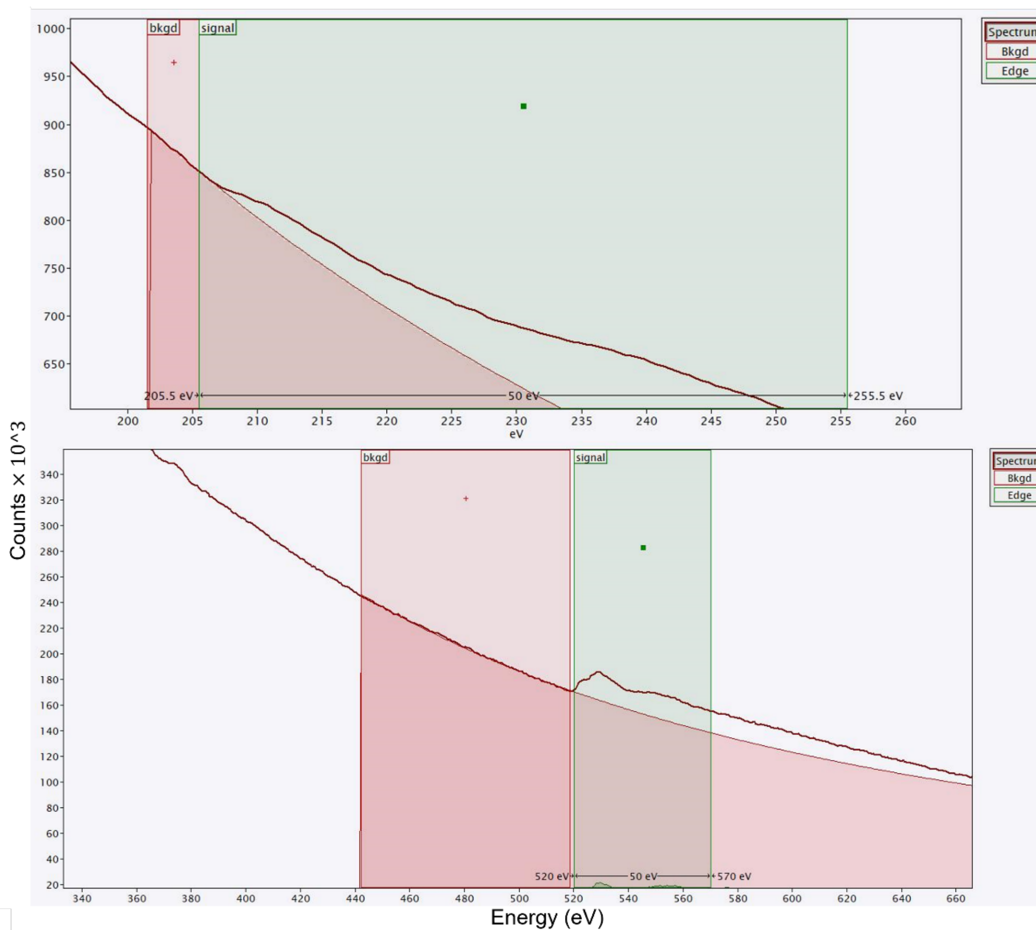

Figure 21 - Signal and background window for dataset 2. The upper panel shows the Nb edge on top and the lower panel shows the oxygen edge.

4.3.2. Data Preparation for Curve Fitting

After acquiring the EELS spectra, oxygen and niobium areal density maps were extracted for both the oxygen K edge and the niobium M edge, using the background fitting and signal integration as described above, and also as described in section 2, applying equations (2.1) and (2.2). This was implemented using Gatan's Digital

Micrograph software. The resulting areal density maps for dataset 1 are presented in Figure 22. These maps provide a visual representation of the distribution of oxygen and niobium in the surveyed area, where brighter pixels indicate a greater areal density (linear grey scale mapping is used). The areal densities extracted for datasets 1 and 2 are presented in an alternative format in Figure 23.

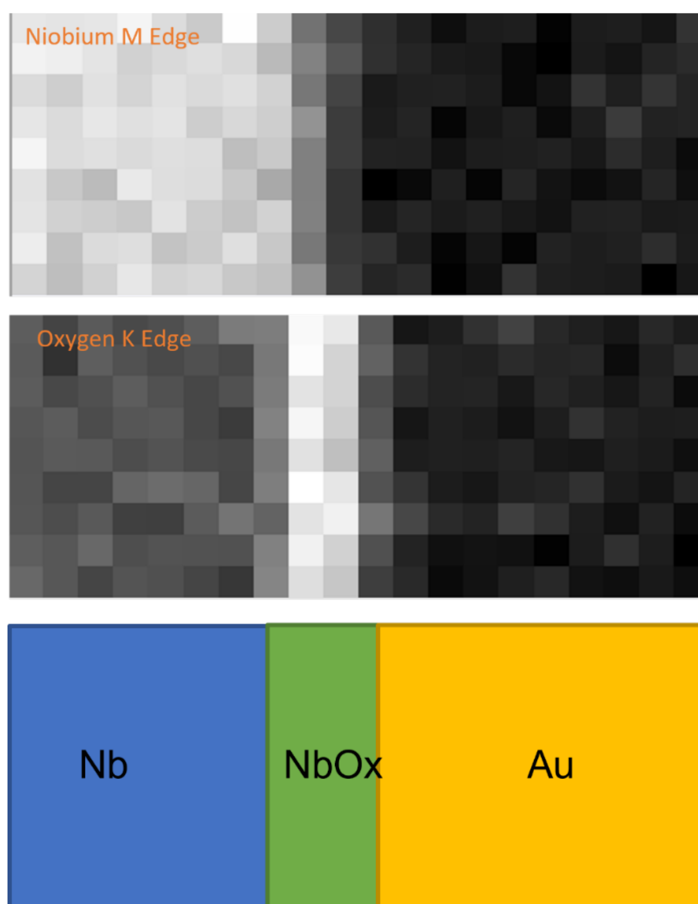

Figure 22 – Grayscale maps showing the relative areal densities of (a) Nb and (b) O for dataset 1 determined from the niobium M and oxygen K edges resepctively, and (c) a schematic image of interface.

The basis of the approach ‘A’ analysis strategy was to look at the variations in the individual niobium and oxygen areal concentrations, rather than the ratio. As also noted peak normalized characteristics were considered, so that the region to the far left in Figure 22 should represent the maximum concentration of Nb, and the right most of edge of oxide region should give the peak oxygen concentration. Effectively layer thickness are then determined by adjusting model parameters to get the best fit upon the peak normalized experimental data. Approach ‘B’ involved the determination of the oxygen-to-niobium areal density ratio and fitting this to model characteristic described in equation (4.7).

In the previous discussion and the model presented in Figure 18, it is stated that there was likely to be some contamination on the sample. From post EELS acquisition secondary electron imaging, it was obvious that the sample had suffered from significant contamination build up, as seen in Figure 24. Attempts were made to remove the carbon contamination using two different cleaning techniques: Ozone combined with deep UV cleaning and argon oxygen plasma cleaning. However, the reduction in carbon contamination provided by these techniques was not significant, perhaps indicating that the contaminated hydrocarbon material had become highly cross-linked. These results indicate that alternative cleaning methods should be considered in order to effectively remove carbon contamination from the surface of materials.

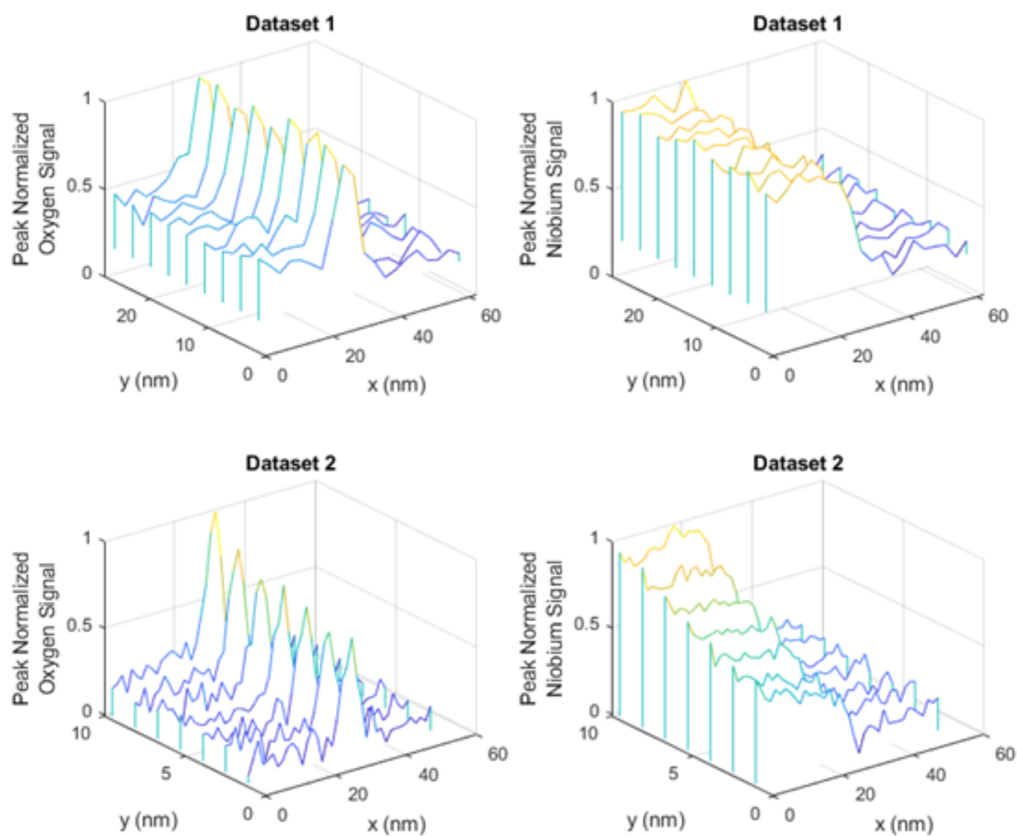

Figure 23 – Plots of the peak normalized data related to the niobium and oxygen areal densities for dataset 1 and 2.

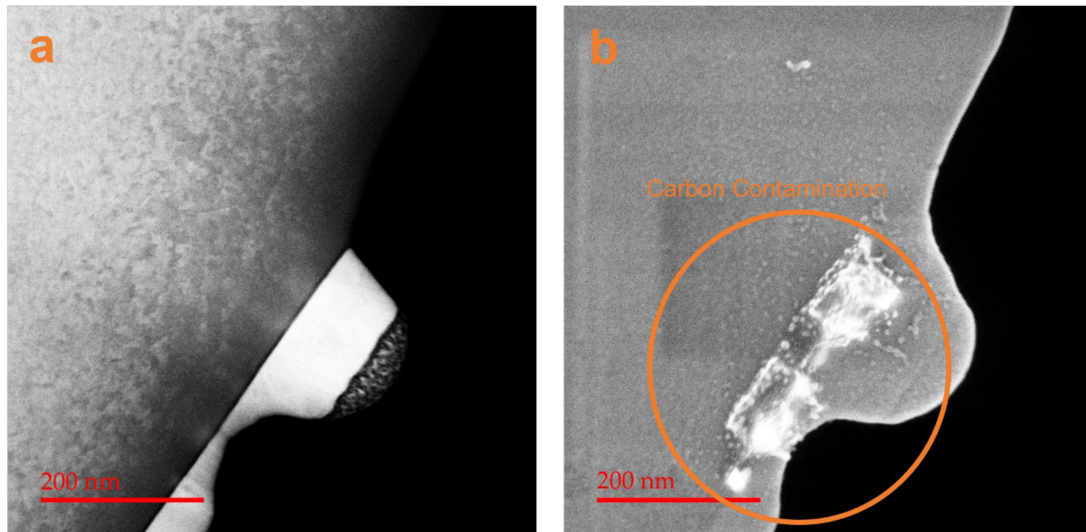

Figure 24 - (a) Dark field image (b) Secondary electron image from the EELS area showing carbon contamination.

4.3.2. Fitting Algorithm

With the experimental data now in hand, and the model described, the task is now to adjust the parameters of the models to minimize the difference between the model and experimental data. The primary aim of this study was to reduce the mean squared error (MSE) between the model and experimental data. The MSE is a commonly used error metric in curve fitting due to its simplicity and robustness to outliers. The formula for the MSE (which is minimised in the fitting process) in approach A is as follows:

$$\min\left\{\begin{array}{c}\sum_{S_{Nb}\in D_{Nb}}\left[\left[U_{Nb}\left(x_s,t_1,t_2,t_3,b_{Nb}\right)\otimes P\left(w,I_{Nb}\right)\right]-S_{Nb}\right]^2+\\ \sum_{S_O\in D_O}\left[\left[U_O\left(x_s,t_1,t_2,t_3,b_O,a_O\right)\otimes P\left(w,I_O\right)\right]-S_O\right]^2\end{array}\right\}/N \quad (4.8)$$

Here S_{Nb} and S_O are the observed normalized areal densities from a line of the data, at a constant y-position and $x = \{x_{(1)}, x_{(2)}, \ldots x_{(N)}\}$, where N are the number of data points in a line. S_{Nb} and S_O are elements of the sets $D_{Nb} = \{S_{Nb(1)}, S_{Nb(2)}, \ldots, S_{Nb(N)}\}$, $D_O = \{S_{O(1)}, S_{O(2)}, \ldots, S_{O(N)}\}$. The dataset lines are presented in Figure 23. Note in this model, that the same width parameter w, and start position parameter, x_s, are used in both the U_O and U_{Nb} functions. Experimentally, S_{Nb} and S_O are collected at range of x and y positions, but here the fits were made only on individual lines where y is constant. This allows us to determine the best fitting background parameters and thickness parameters with respect to the y-direction which runs parallel the surface. For example, looking at the Nb signal of dataset 2 in Figure 23 it is obvious that there is a significant variation in background parameters for example, going from line to line.

For approach B, the minimized MSE was given by:

$$\min\left\{\sum_{S_{O:Nb}\in D_{O:Nb}}\left[\left[U_{O:Nb}\left(x_s,t_1,t_2,t_3,a_{O:Nb},b_{O:Nb}\right)\otimes P\left(w,I_{Nb:0}\right)\right]-S_{O:Nb}\right]^2+\right\}/N \quad (4.9)$$

where $S_{O:Nb}$ is the O:Nb areal density ratio determined from dividing O and Nb areal densities presented in Figure 23. Again, the summation is taken over all elements in line of dataset taken at constant y.

The preliminary stages of the fitting procedure were aimed at evaluating a variety of fitting algorithms. The general purpose non-linear least squares minimization method, "lsqnonlin," along with the Simulated Annealing algorithm and the Genetic Algorithm, were investigated in this study. All algorithms were implemented in MATLAB. The lsqnonlin method uses a trust region reflective (TRR) algorithm. More detail on this can be found in the MATLAB documentation. In essence this algorithm minimizes multivariate functions by breaking the function down to quadratic surface approximations operating on basis vectors that approximate the original problem. In the testing of algorithms here, the main aim was to determine which algorithm works best rather than gain a complete understanding of how they work. Thus here, we refer the interested reader to the MATLAB documentation to understand the full details of the algorithm. In essence though, this algorithm can work on some non-linear problems, such as ours, provided they are not too non-linear.

The simulated annealing algorithm is a metaheuristic optimization algorithm inspired by the process of annealing in metallurgy, where a metal is heated and then slowly cooled to increase its strength and durability. Fitting with Simulated Annealing starts with an initial guess for the model parameters and then iteratively adjusts the parameters to minimize the cost function. After a certain ‘cooling’ time, related to some parameter defining a number of regular refinement steps, the algorithm randomly perturbs the current parameters and starts refining the solution again. If the new cost is lower than the current cost, the new parameters are accepted as the new current state. However, if the

new cost is higher than the current cost, the new parameters are accepted with a probability that decreases as the temperature decreases.

The Genetic Algorithm (GA) fitting is an optimization technique that uses the principles of natural selection and genetics to find the optimal set of parameters that minimize a cost function. The GA fitting process starts with an initial population of candidate solutions, each of which is represented by a set of parameters that determine the behavior of the model. The fitness of each candidate solution is evaluated by computing the cost function, which measures how well the model fits the data.

The results of the fitting comparison between the three algorithms an average of all the lines using approach B is given in Figure 25 (a, b) for datasets 1 and 2, respectively. The regions displayed on the top of the plots correspond to the area of the respective plots. The resulting MSE are given in Table 7.

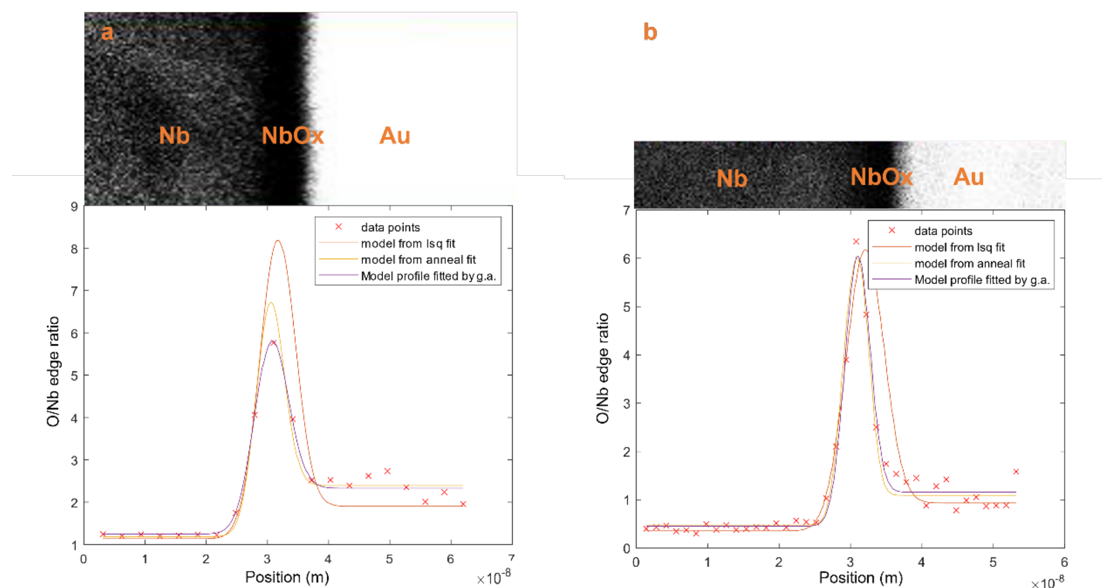

Figure 25 - Fitting results with three algorithms: (i) trust region reflective (MATLAB 'lsqnonlin'), (ii) annealing method, and (iii) genetic algorithm.

Table 7 – Minimum MSE achieved with different algorithms for datasets 1 and 2 and fitting approach B.

Dataset	Dataset 1			Dataset 2		
Algorithm	TRR	Simulated Annealing	Genetic Algorithm (GA)	TRR	Simulated Annealing	Genetic Algorithm (GA)
Mean Squared Error	6.61E-1	7.65E-2	2.75E-2	4.44E-1	5.24E-2	4.24E-2

For both datasets the genetic algorithm (GA) gave the lowest MSE. Thus, the GA was selected as the optimization technique going forward due to its superior performance in terms of error minimization compared to the other two algorithms. In many ways this was

expected as the algorithm has a well-known strong ability to handle highly non-linear models, multi-modal problems, and problems with multiple local minima.

4.3.3. Results of Fitting

Approach A

In approach A, the fitting procedure was performed on the areal density maps of niobium and oxygen, row by row. An example fit is shown in Figure 26. Example extracted thicknesses of the oxide layers at each *y*-position through the samples from a single run of the genetic algorithm (GA) are presented in Figure 27 for dataset 1 and Figure 28 for dataset 2. In these plots the total height of the bars is the total thickness. The plots of Figure 27 and Figure 28 give the *y*-position in the EELS acquisition region. Noting the × 3.1 at right hand of Figure 27, the *y*-position difference between bars 1 and 2 is 3.1 nm for example. This is also the step size given in Table 6.

In addition, we seeded the GA solver with a range of randomly selected start points to see if the algorithm consistently minimized the MSE to give the same parameter values. Of particular interest are the parameters related to the thicknesses of the niobium oxides. Given that we had a relatively large number of parameters, within quite a complex model, and relatively few data points in each line, it seems plausible that were many local minima within the parameter space. Also, it was possible that these local minima vary only slightly in value from each other.

Indeed, we found that running the GA solver many times on a single line yielded a range of thickness parameters. For each line, we determined the mean of the thickness parameters as determined from 19 runs of the solver, then in Table 8 we give the mean extracted thickness, $\bar{T}$, defined through

$$\mu_j = \frac{\sum_{i=1}^{m} t_i}{m} \qquad \sigma_j = \sqrt{\frac{\sum_{i=1}^{m}\left(t_i - \mu_j\right)^2}{m}}$$
$$\bar{T} = \frac{\sum_{j=1}^{n} \mu_j}{n} \qquad u = \sqrt{\frac{\sum_{j=1}^{n}\left(\mu_j - \bar{T}\right)^2}{n}} \qquad v = \sqrt{\frac{\sum_{j=1}^{n}\sigma_j^{\,2}}{n}}. \tag{4.10}$$

Here, *m* represents the number of GA solver runs performed on a single line, with each solver run on a line having index *i*, and *n* is the number of lines in the dataset, with each line having index *j*. Here, *u* represents the standard deviation of a line's mean thickness parameters averaged over all the lines. It should be compared to v^2, which is the average of the variances squared for each line, giving a measure of the reliability and error in any single extracted thickness parameter for a single line. When $v < u$, *u* may be taken as characterizing the degree of interface roughness. Entries in Table 8 are of form $\bar{T}$ [*u*, v]. The variances of the thicknesses for each line (σ_j) were determined from analysing the results of 19 runs of the GA algorithm on each line, i.e. $m = 19$. For now, we note that these deviations values are relatively large, and will come back to discussing the implications of this after presentation of the results of approach B.

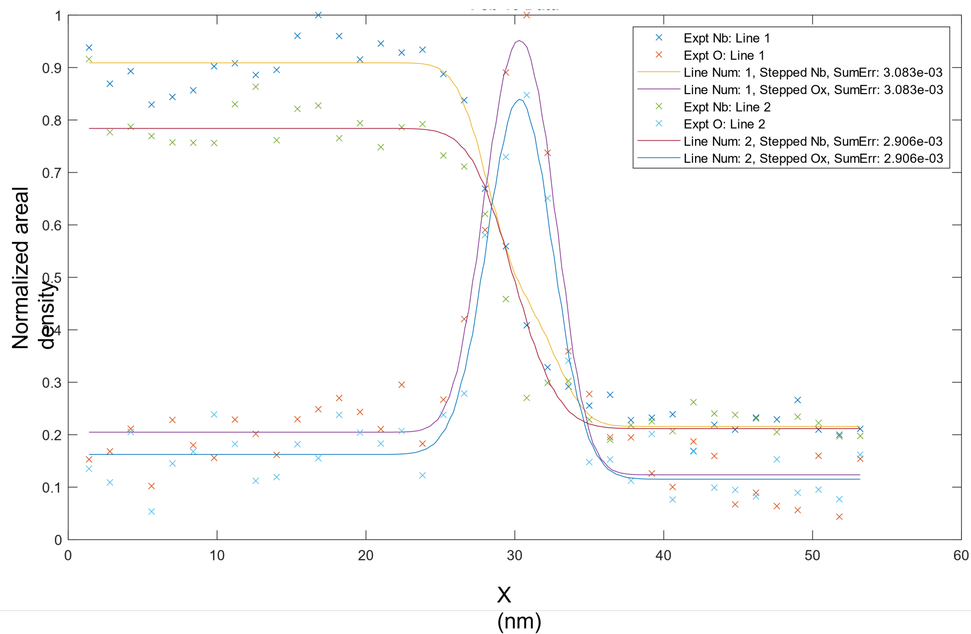

Figure 26 – Sample fitting on the first two rows of the areal densities of oxygen and niobium for dataset 2.

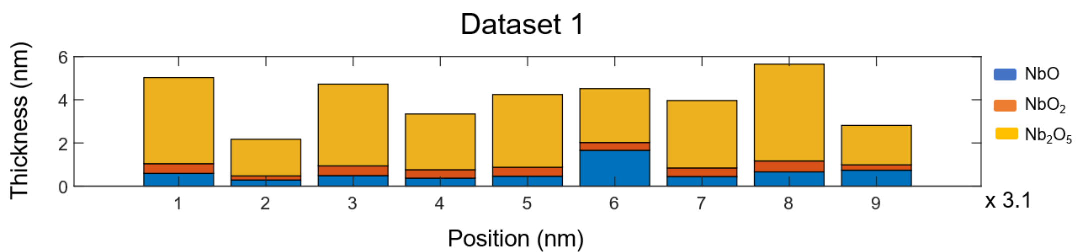

Figure 27 – Example extracted thicknesses with the model fitting on dataset 1 with approach A.

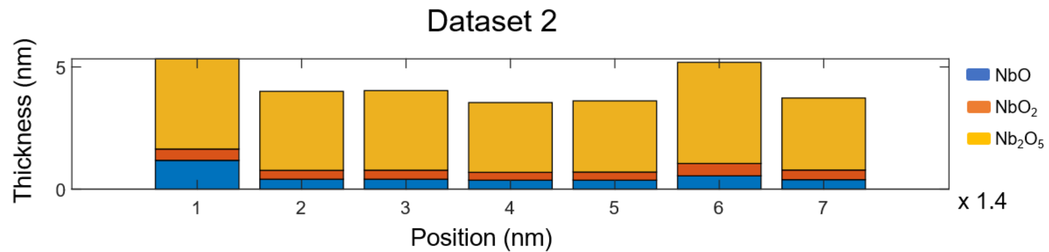

Figure 28 – Example extracted thickness with the model fitting on dataset 2 with approach A.

Table 8 – Extracted average thicknesses from the datasets with approach A. Thickness entries in the table have the form *T* [*u*, *v*], where *T* is the mean thickness, *u* is the standard deviation of the means across all lines, and *v* is an error estimate on a single line, averaged over all lines. The average MSE is the mean over all lines of the mean squared error between the fitted curves and experimental data.

Dataset	Total thickness (nm)	NbO thickness (nm)	NbO_2 thickness (nm)	Nb_2O_5 thickness (nm)	Average MSE
1	4.23 [0.28, 0.96]	0.34 [0.12, 0.26]	0.26 [0.10, 0.23]	3.63 [0.35, 0.83]	2.37E-3
2	4.02 [0.20, 1.00]	0.49 [0.25, 0.39]	0.29 [0.17, 0.21]	3.24 [0.42, 0.77]	3.45E-3

Looking at the average MSE in Table 8, where the mean of individual MSEs were taken for each line, it can be seen that its value is smaller than the error in Table 7. The initial

tests, in Table 7, were performed on an average of all lines, rather that working on a line-by-line basis. It is observed that the average mean squared error (MSE) is improved by working on a line-by-line basis. Strictly speaking, Table 7 should be compared with the results of approach B, applied on a line-by-line basis, as will be discussed (see Table 9), though the same trend applies.

Based on HR-TEM images taken from the sample, such as in Figure 14, the thickness of the oxide layer was estimated to be approximately 4 to 5 nm which is in reasonable agreement with the results of the curve fitting, though the thickness from curve fitting is perhaps a little smaller. The major oxide component in the NbO_x layer is also Nb_2O_5, as expected. Paying closer attention to Figure 14, there is some variation in total thickness, approximately from 3.5 to just over 5 nm, which appears approximately in agreement with the u values given in Table 8. However, though Figure 14 shows us this variation in total thickness, it does not tell us about the variations of NbO or NbO_2 thicknesses, whereas the results here do tell us something. For future studies the standard deviation of these thickness measurement parameters, particularly the 'u' measure given through Equation 4.10, would possibly be a useful means to make comparisons between different film surface oxides.

Approach B

An example of fitted characteristic using approach B are presented in Figures 29 and 30, along with a summary extracted thicknesses in Table 9. It is noted that the total thickness

calculated based on this model approach are slightly less than the thickness of the oxide layer observed in HR-TEM, or as extracted from Approach A. Likely this is due to the very misleading information that is provided in the ratio data at the right hand side of these plots, where the data here comes from dividing two small and noisy numbers, which in turn generates a larger even noisier number. As observed in the previous analysis, an undefined ratio of 0/0 would be present in the ideal scenario. Consequently, any signals perceived in this area are potentially attributed to setup errors or noise. Moreover, using the ratio as a fitting parameter involves incorporating less data into the model fitting method, which has a higher error margin (owing to being a ratio) compared to approach B. Thus, approach B would be expected to be less reliable than approach A. This is also evident in the visually poorer quality of fit seen in Figures 29 and 31, and that the average MSE from the fits on the lines is less for approach B than approach A, as seen in Table 9.

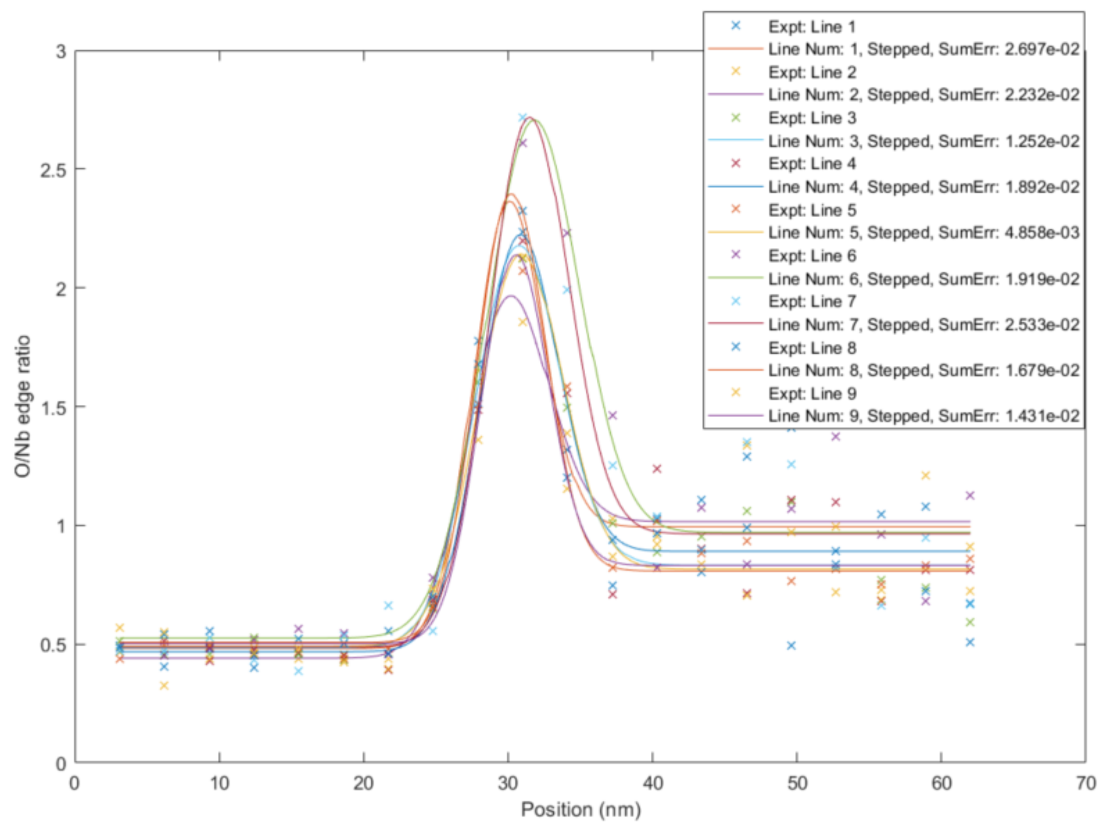

Figure 29 – Fitted models for dataset 1 with approach B.

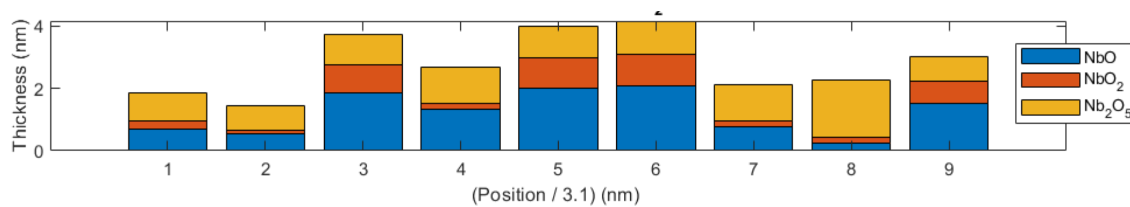

Figure 30 – Example extracted thickness with model fitting on dataset 1 with approach B.

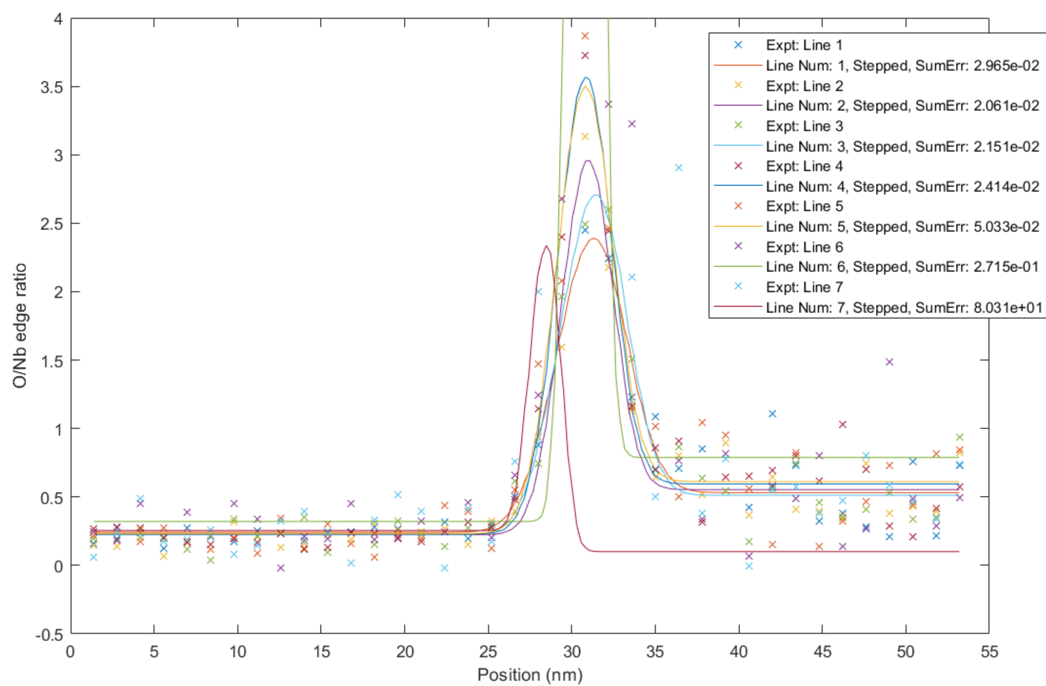

Figure 31 – Fitted models for dataset 2 with approach B

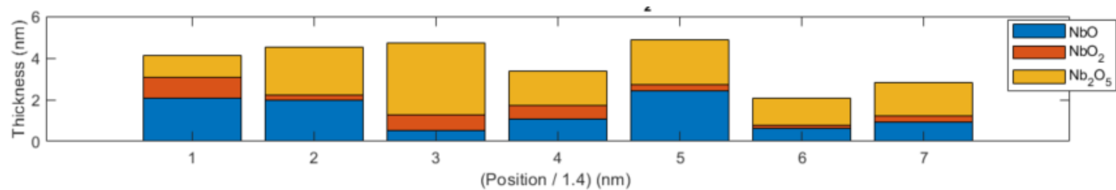

Figure 32 – Example extracted thickness with the curve fitting on dataset 2 with approach B.

Table 9 - Summary of mean extracted thicknesses from the datasets for both approaches. Thickness entries in the table have the form *T* [*u*, *v*], where *T* is the mean thickness, *u* is the standard deviation of the means across all lines, and *v* is an error estimate on a single line, averaged over all lines (see Eqn. (4.10)).

Dataset / Approach	Total thickness (nm)	NbO thickness (nm)	NbO_2 thickness (nm)	Nb_2O_5 thickness (nm)	Average MSE
1/A	4.23 [0.28,0.96]	0.34 [0.12, 0.26]	0.26 [0.10, 0.23]	3.63 [0.35,0.83]	2.37E-3
2/A	4.02 [0.20, 1.00]	0.49 [0.24, 0.39]	0.29 [0.16, 0.20]	3.24 [0.42, 0.77]	3.45E-3
1/B	3.12 [0.70, 0.74]	1.20 [0.41, 0.52]	0.46 [0.27, 0.24]	1.48 [0.15, 0.36]	1.79E-2
2/B	2.66 [0.60, 0.68]	1.10 [0.29, 0.49]	0.62 [0.15, 0.25]	0.93 [0.20, 0.20]	11.5

Nevertheless, the observations indicate that fitting dataset 2 using approach B on a line-by-line basis results in a higher average mean squared error (MSE) than fitting to the average of all the lines, as is presented in Table 7. This is due to lines 6 and 7 in Dataset 2, which as they contain the ratio of small (noisy) numbers give some large ‘outlier’ values. Attempts to fit to this data are thus misleading, and give a very large MSE, which thus strongly affects the average MSE over all the lines. For the analysis in Table 7, all the lines were averaged before fitting, so these few outlier points were dampened and brought back into a range where a reasonable fit could be achieved. This illustrates the

advantage of approach A: the noise and likelihood of outliers in the data is much reduced. Hence, approach A is recommended for subsequent investigations.

Here, as in Table 8, entries Table 9 are of the form, $\bar{T}$ [u, v], as defined in Equation 4.10 and found from all a series of solver runs, where again we set m = 19. In all cases we see that the single line based standard deviation, v, is very similar to $\bar{T}$ for the NbO and NbO_2 layers. Also, we see that the NbO and NbO_2 extracted layer thickness come very close to the lower bound specified in the GA solver, which was set at 0.05 of the total thickness. Ideally we would like v to better than 0.15 nm, and it should be further verified that the thickness of these layers is not influenced by the lower bound value on the solver. At this stage this work has not been done, and we deem v to likely be too large to allow us to place much confidence in the values of the NbO and NbO_2 layer thickness extracted from single lines. For example, with Dataset 2, method A, the NbO thickness has an approximate one standard deviation error of ± 80%. This means our data gives a significant probability to there being no NbO layer present, whereas other studies indicate that there must certainly be NbO present.

To achieve greater certainty in our NbO and NbO_2 layer thicknesses, we would need significantly more data points in our line profiles, and possibly reduced Poisson noise in our individual data points, which is achieved by using a greater a greater electron dose per pixel. Another possibility would be to use a modified model whereby we assume that the thickness parameters and spread function width are the same on all lines, letting only

the background parameters and start position vary from line to line. Then the optimization could be performed on the entire dataset. In this way the fitting would simultaneously use many more data points and less parameters, and so give reduced uncertainty in the thickness parameters.

However, we did not investigate this further here, as the main purpose of our investigation was to show that our new approach of simultaneously fitting on the individual elemental concentrations (approach A) gives significantly more reliable and useful results than the ratio method (approach B) which is currently and normally used in EELS analysis of thin layers like this.

With the thickness parameters extracted, it is feasible to examine the EELS signals in an ideal scenario without any background signals by setting the a and b parameters to zero, if desired. The results of this are shown in Figure 33 for a line taken dataset 1, showing the O:(Nb+O) and Nb:(Nb+O) areal density ratios.

In Figure 33-(a), the extracted oxygen signal has a peak that is very close to the centre of the oxide region, marked by vertical solid and dashed lines. Also as expected the Nb signal drops off across the layer. Looking at Figure 33-(b) and (c), the ratios appear to look like a Gaussian convolved with a step function as expected, where the step onset occurs at the edge of the Nb. The shapes of the ratio plots in (Figure 33 (b) and (c)) are consistent with the behavior of the Nb:(Nb+O) ratio seen in a prior STEM EELS study

[27], which is reproduced in Figure 34. On the plots (Figure 33) horizontal lines are shown to indicate the ratios that correspond to NbO, NbO_2 and Nb_2O_5.

However, in particular look at the color scale of the righthand part of Figure 34. Here the authors attempt to mark the levels for NbO, NbO_2 and Nb_2O_5, and hint through the color scale that they thus have a mapping for the various oxide types. Layer thickness are then inferred from this. From the model results presented in Figure 33, in fact there is no direct meaning that can be taken from where levels intersect the ratio curves. Intersection points do not indicate the actual positions of the interfaces and the thickness of the layers: the intersections of the red and black horizontal lines in Figure 33, do not also intersect with the ratio curves.

This also illustrates why this study and modelling approach was started. Though EELS is a powerful technique, it is only as good as the analysis technique. Simple presentations and analysis can (and do) lead to seriously misleading results. For the critical field of study of the structure of niobium oxides this is not acceptable. Better and more robust analysis techniques such as done here are needed.

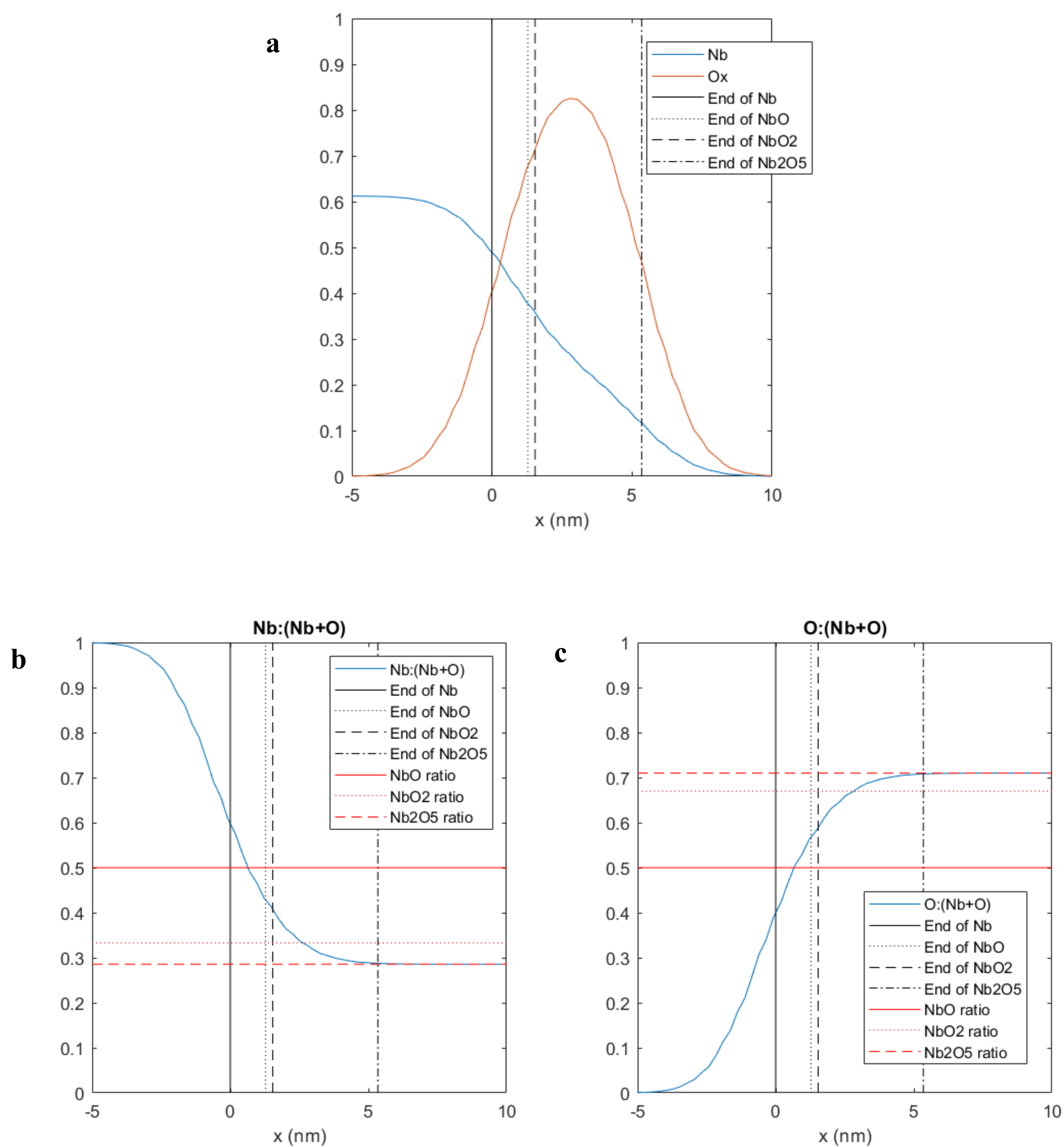

Figure 33 - Background-removed (a) Nb and O signals, (b) Nb:(Nb+O) ratio and (c) O:(Nb+O) ratio for line 1 of dataset 1, fitted using approach A.

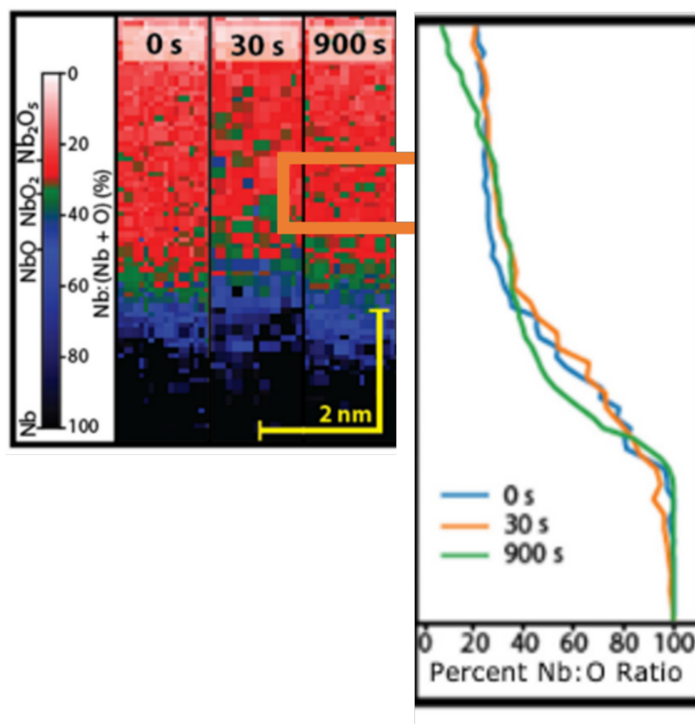

Figure 34 - STEM-EELS data on the niobium oxide interface (a) Niobium oxide Nb:(Nb + O) EELS maps as a function of the etch time (b) Depth profiles derived from EELS spectra, taken from Altoé *et al*[27].

In summary, the methodology proposed in this study presents a method to extract some physically meaningful parameters from curves and EELS data. This removes the need for a human operator to subjectively 'guess' layer thicknesses from shape of the curves, and thus presents a method to simplify the comparison of EELS data collected from NbO_x layers prepared under different conditions, and in different laboratories etc. The model employed in this study allows for removal of background signals and errors and avoids having to work directly with the ratio of niobium to oxygen concentrations. Working with

this ratio directly can be problematic as taking ratio of two small numbers both of which have significant error can result in larger error in the ratio. Thus, more reliability was found in simultaneously fitting to the normalized Nb and O areal densities, defined through equation (4.8).

This method accounts for both surface oxidation of the lamella on the niobium side and the effect of contamination on EELS data. An additional advantage of this method is that it does not require careful calibration of a perfect sample. The results of this study provide valuable insights into the oxide layer of niobium and represent a significant step forward in understanding the microstructure of two-level systems. Further investigation can be done to comprehend the complexities of this system in the future.

Chapter 5: Conclusion

The primary objective of this thesis is to enhance the comprehension of the microstructure of the niobium oxide layer at the interface of the niobium, as this layer plays a critical role in energy relaxation in niobium-based devices owing to the presence of two-level system (TLS) defects. This study proposed a novel method to determine the material composition related to the variation of niobium oxide in the NbO_x layer.

The present study utilized electron energy loss spectroscopy (EELS) as a characterization method. EELS was selected due to its heightened precision, particularly when examining light elements, in contrast to other methodologies such as energy dispersive X-ray spectroscopy (EDS). Moreover, EELS is distinguished by its superior resolution.

In this investigation, as the sample was a bulk material, it was necessary to create a lamella to enable visualization under the electron microscope. The lamella was prepared utilizing a focused ion beam machine (FIB), with the objective of creating an electron-transparent specimen possessing a thickness of approximately 50 nm. Given that the focus of this investigation pertained to the surface oxide layer, it was critical to safeguard it from the ion beam damage. In light of this, a dual layer consisting of gold and platinum was employed to shield the layer. Subsequently, multiple transmission electron microscope images were captured from the sample, thereby finding the thickness of the NbO_x layer to be approximately 4-5 nm.

Subsequently, electron energy loss spectroscopy (EELS) was performed on the lamella obtained from the interface of niobium and gold. Suspecting that the current methods of EELS analysis on the surface oxide layer, which simply looks at the ratio of the recorded Nb and O areal density, had deficiencies and could be improved to extract more meaningful parameters related to the thicknesses of its components, a model-based approach was developed and investigated. Two models were investigated: one that modelled and fitted the individual areal densities simultaneously, and another that just modelled and fitted the ratios of the areal densities. These models took account of important background and sample contamination effects which are usually ignored in EELS analysis on the assumption that the sample can be kept clean enough for the duration of the experiment, which was certainly not true in this work. Also, the extended size of the sampling function was taken into account which occurs due to the significant thickness of the sample and the roughness of the interfaces.

Having established that the best performance in fitting the model parameters was achieved through the use of a genetic algorithm, a subsequent discovery was made regarding the reliability of an alternative approach. Specifically, it was observed that fitting the individual areal densities offered greater reliability compared to direct analysis of the purported O:Nb ratio. This particular methodology appears to be unutilized by other practitioners in the field of electron microscopy, with respect to the determination of surface oxide layer properties of Nb or other comparable systems.

Based on underlying models, the areal densities of Nb and oxygen were developed, wherein the thickness of each layer was treated as a variable in this study.

The output of the model fitting analysis yielded the total thickness of the oxide layer, as well as the thickness of each of the distinct niobium oxide species comprising the layer. While these thickness results were broadly consistent with previous research findings, it was demonstrated that some current methods being adopted in the literature to extract layer thickness from EELS data are at best very suspicious and more likely incorrect. This research demonstrated this by looking at the model response of an idealized experimental data where the fitted background signals were remove. This showed that the intersection of threshold levels cannot be taken to infer layer thicknesses.

All this presents a step forward in being able to do detailed microstructural characterisation of the surface oxide layer of any material. In time it is hoped that the useful thickness parameters it provides can be correlated with other effects and observations of niobium resonators in order to get better understanding of the possible structure of the two level systems that limit their performance and quality factor. Given more time for this study, the newly developed technique would have been applied to a range of materials prepared under different conditions as provided from superconducting RF cavities, and a search would have been done to find the correlations between quality factors and the thickness parameters for example.

Bibliography

[1] K. Fossheim and A. Sudbø, "Superconductivity : physics and applications," pp. 427. West Sussex, U.K.: Wiley, 2004.

[2] Y. Takai, T. Ando, T. Ikuta, and R. Shimizu, "Principles and Applications of Defocus-Image Modulation Processing," *Scanning Microsc.*, vol. 11, pp. 391–405, 1997.

[3] D. R. Tilley and J. Tilley, "Superfluidity and Superconductivity", American Journal of Physics, vol. 44, pp. 608–609, 1976.

[4] D. Dominguez, E. A. Jagla, and C. A. Balseiro, "Phenomenological Theory of the Paramagnetic Meissner Effect," Phys. Rev. Lett. vol. 72, pp. 2773, 1994.

[5] C. Kittel, "Introduction to Solid State Physics, 8th edition." New York: Wiley, 2004.

[6] R. Hott, G. Zwicknagl, R. Kleiner, T. Wolf, and G. Zwicknagl, "Review on Superconducting Materials," 2013. Available: https://www.researchgate.net/publication/237000459 [Acessed May 24, 2023].

[7] Grassellino, Anna, "Field-dependent losses in superconducting niobium cavities", Ph.D. Dissertation, Dept. of Physics and Astronomy, University of Pennsylvania, Filadelphia, PA, 2011.

[8] Y. Furuto, “Fundamentals of Niobium Based Superconductors”, in Niobium - Proceedings of the International Symposium, p. 445, Metallurgical Society of AIME, Warrendale, PA, 1984.

[9] S. Uejo, "Niobium based Intermetallic Compound for High-Temperature Structural Material", Shigen-to-Sozai, vol. 110, pp. 843-849, 1984.

[10] C. Nico, T. Monteiro, and M. P. F. Graça, “Niobium oxides and niobates physical properties: Review and prospects,” *Progress in Materials Science*, vol. 80, pp. 1–37, July 2016.

[11] A.-M. Valente-Feliciano, “Superconducting RF materials other than bulk niobium: a review,” Supercond. Sci. Technol. vol. 29, 113002, 2016.

[12] F. Jazaeri, A. Beckers, A. Tajalli, and J.-M. Sallese, “A Review on Quantum Computing: Qubits, Cryogenic Electronics and Cryogenic MOSFET Physics”, in 2019 MIXDES - 26th International Conference "Mixed Design of Integrated Circuits and Systems", pp. 15-25, Rzeszow, Poland, 2019.

[13] H. R. Khan, C. J. Raub, W. E. Gardner, W. A. Fertig, D. C. Johnston, and M. B. Maple, “Magnetic and superconducting properties of niobium oxides,” *Mater. Res. Bull.*, vol. 9, pp. 1129–1135, Sep. 1974.

[14] N. Gorgichuk, T. Junginger, and R. de Sousa, “Modelling dielectric loss in superconducting resonators : Evidence for interacting atomic two-level systems at

the Nb/oxide interface", Phys. Rev. Appl. vol. 19, 024006, 2023.

[15] J. Pelleg, "Imperfections (Defects) in ceramics," in Mechanical Properties of Ceramics. Solid Mechanics and Its Applications, vol. 213. Springer, Berlin, 2014, pp. 179–213.

[16] M. E. Flatté and J. M. Byers, "Local Electronic Structure of Defects in Superconductors," Solid State Phys., vol. 52, pp. 137–228, 1999.

[17] C. Z. Antoine, "Influence of crystalline structure on RF dissipation in Niobium: flux trapping, hydride precipitate, doping behavior", arXiv:1802.07241 [physics.acc-ph], 2018.

[18] A. V Narlikar and D. Dew-Hughes, "The Effect of Dislocation Configuration on the Superconducting Properties of Niobium and Vanadium", phys. stat. sol. (b), vol. 6, pp. 383-390, 1964.

[19] K. Zhussupbekov *et al.*, "Oxidation of Nb(110): atomic structure of the NbO layer and its influence on further oxidation," *Sci. Rep.*, vol. 10, 3794, 2020.

[20] R. W. Simon, C. E. Platt, and A. E. Lee, "Low-loss substrate for epitaxial growth of high-temperature superconductor thin films", *Appl. Phys. Lett*, vol. 53, pp. 2677-2679, 1988.

[21] R. Barends *et al.*, "Niobium and Tantalum High Q Resonators for Photon Detectors," in *IEEE Trans. Appl. Supercond.*, vol. 17, pp. 263-266, 2007.

[22] C. Wang *et al.*, "Surface participation and dielectric loss in superconducting qubits", *Appl. Phys. Lett*, vol. 107, 162601, 2015.

[23] J. Gao *et al.*, "Experimental evidence for a surface distribution of two-level systems in superconducting lithographed microwave resonators," *Appl. Phys. Lett.*, vol. 92, 152505, Apr. 2008.

[24] G. Calusine *et al.*, "Analysis and mitigation of interface losses in trenched superconducting coplanar waveguide resonators," *Appl. Phys. Lett.*, vol. 112, 062601, Feb. 2018

[25] C. Wang, C. Axline, and Y. Y. Gao, "Surface participation and dielectric loss in superconducting qubits", *Appl. Phys. Lett*, vol. 107, 162601, 2015.

[26] M. Checchin *et al.*, "Frequency dependence of trapped flux sensitivity in SRF cavities," *Appl. Phys. Lett.*, vol. 112, no. 7, 072601, 2018.

[27] M. V. P. Altoé *et al.*, "Localization and Mitigation of Loss in Niobium Superconducting Circuits," *PRX Quantum*, vol. 3, no. 2, 020312, 2022.

[28] N. Gorgichuk, T. Junginger, and R. de Sousa, "Modeling Dielectric Loss in Superconducting Resonators: Evidence for Interacting Atomic Two-Level Systems at the Nb/Oxide Interface," *Phys.Rev.Applied*, vol. 19, no. 2, 024006, 2023.

[29] M. Delheusy *et al.*, "X-ray investigation of subsurface interstitial oxygen at Nb/oxide interfaces," *Appl. Phys. Lett.*, vol. 92, no. 10, 101911, 2008.

[30] T. L. Daulton, K. S. Bondi, and K. F. Kelton, "Nanobeam diffraction fluctuation electron microscopy technique for structural characterization of disordered materials—Application to $Al_{88-x}Y_7Fe_5Ti_x$ metallic glasses," *Ultramicroscopy*, vol. 110, no. 10, pp. 1279, 2010.

[31] A. A. Murthy *et al.*, "Developing a Chemical and Structural Understanding of the Surface Oxide in a Niobium Superconducting Qubit," *ACS Nano*, vol. 16, no. 10, pp. 17257–17262, 2022.

[32] R. E. Gordon, "Electron microscopy: a brief history and review of current clinical application," *Methods Mol. Biol.*, vol. 1180, pp. 119–135, 2014.

[33] M. Tsuji, "Electron Microscopy," *Compr. Polym. Sci. Suppl.*, vol. 1, pp. 785–840, 1989.

[34] P. J. R. Uwins, "Environmental scanning electron microscopy," *Met. forum*, vol. 18, pp. 51–75, 1994.

[35] S. Zaefferer, "A critical review of orientation microscopy in SEM and TEM," *Cryst. Res. Technol*, vol. 46, no. 6, pp. 607–628, 2011.

[36] K. Murata and M. Wolf, "Cryo-electron microscopy for structural analysis of dynamic biological macromolecules," *Biochim. Biophys. Acta - Gen. Subj.*, vol. 1862, no. 2, pp. 324–334, 2018.

[37] O. Wilhelmi, S. Reyntjens, B. Van Leer, P. A. Anzalone, and L. A. Giannuzzi, "Focused Ion and Electron Beam Techniques," in *Handb. Silicon Based MEMS Mater. Technol.*, V. Lindroos, Ed., William Andrew Publishing, pp. 323–325, 2010.

[38] K. Narayan, S. Subramaniam. "Focused ion beams in biology", *Nat Methods*, vol 12, pp 1021–1031 (2015).

[39] W. Giurlani, E. Berretti, M. Innocenti, and A. Lavacchi, "Measuring the Thickness of Metal Films: A Selection Guide to the Most Suitable Technique," p. 12, 2020.

[40] R. F. Egerton, "Electron energy-loss spectroscopy in the TEM," *Reports Prog. Phys.*, vol. 72, no. 1, 2009.

[41] D. C. Joy and D. M. Maher, "The quantitation of electron energy loss spectra," *J. Microsc.*, vol. 124, no. 1, pp. 37–48, 1981.

[42] R. D. Leapman and C. R. Swyt, "Separation of overlapping core edges in electron energy loss spectra by multiple-least-squares fitting," *Ultramicroscopy*, vol. 26, p. 393, 1988.

[43] G. Kothleitner and F. Hofer, "Optimization of the signal to noise ratio in EFTEM elemental maps with regard to different ionization edge types," *Micron*, vol. 29, no. 5, pp. 349–357, 1998.

[44] J. Verbeeck, S. Van Aert, and G. Bertoni, "Model-based quantification of EELS spectra: Including the fine structure," *Ultramicroscopy*, vol. 106, no. 11–12, pp. 976–980, 2006.

[45] K. Riegler and G. Kothleitner, "EELS detection limits revisited: Ruby - a case study," *Ultramicroscopy*, vol. 110, no. 8, pp. 1004–1013, 2010

[46] P. J. Thomas and R. D. Twesten, "A Simple, Model Based Approach for Robust Quantification of EELS Spectra and Spectrum-Images," *Microsc. Microanal.*, vol. 18, no. S2, pp. 968–969, 2012.

[47] A. Grassellino *et al.*, "Unprecedented quality factors at accelerating gradients up to 45 MVm^{-1} in niobium superconducting resonators via low temperature nitrogen infusion", *Supercond. Sci. Technol.,* vol. 30, 094004, 2017.

[48] D. A. Turner, G. Burt, and T. Junginger, "No interface energy barrier and increased surface pinning in low temperature baked niobium," *Sci. Rep.*, vol. 12, no. 1, pp. 1–9, 2022.

[49] J. Verjauw *et al.*, "Investigation of Microwave Loss Induced by Oxide Regrowth in High- Q Niobium Resonators", *Phys. Rev. Appl.*, vol. 16, no. 1, pp. 1–14, 2021.

[50] S. Stallinga *et al.*, "Accuracy of the Gaussian Point Spread Function model in 2D localization microscopy," *Opt. Express,* vol. 18, no. 24, pp. 24461–24476, 2010.

[51] Minin, I.V., & Minin, O.V., "Diffractional Optics of Millimetre Waves", Boca Raton: CRC Press, 2004.

[52] K. He, N. Chen, C. Wang, L. Wei, and J. Chen, "Method for Determining Crystal Grain Size by X-Ray Diffraction," *Cryst. Res. Technol.*, vol. 53, no. 2, 1700157, 2018.

[53] J. L. Jorda, R. Flukiger, and J. Muller, "A New metallurgical investigation of the niobium-aluminium system," *J. Less Common Met.*, vol. 75, no. 2, pp. 227–239, 1980.

Appendix A - Characterizing Crystallinity and Grain Size of Treated Bulk Niobium Samples using X-Ray Diffraction (XRD)

Introduction to XRD

X-ray diffraction (XRD) is one of the common techniques that is used to determine the crystallite size of materials. Crystallite size or grain size refers to the average size of the crystallites in a material and is an important factor that can affect the physical and mechanical properties of the material.

X-ray diffraction machine operates by directing a focused, single-wavelength X-ray beam at a sample, then measuring the X-rays that are scattered at various angles. The beam is usually produced by an X-ray tube, which uses electricity to excite metal targets, such as copper or cobalt, to generate X-rays. The sample is positioned on a rotating platform in front of the beam and the scattered X-rays are measured by a detector, such as a scintillation counter or a CCD detector. The XRD machine has three main parts which include the X-ray source, the sample holder, and the detector. X-ray diffraction is based on Bragg's Law, which posits that when an X-ray beam is directed at a crystal, the waves scattered by the crystal will reflect it in a specific direction. The angle of this reflection is determined by the distance between the atomic planes of the crystal and the wavelength of the X-rays [51]. According to Bragg’s Equation:

$$n\lambda = 2dsin\theta,$$

where, “n” is the order of the diffraction, λ is wavelength, d is lattice spacing, and θ is diffraction angle.

The material crystallite size can be determined through the measurement of the full width at half maximum (FWHM) of the diffraction peaks in the XRD pattern. The FWHM is related to the size of the crystallites, with smaller FWHM values indicating larger crystallite sizes. One of the most common ways to calculate crystallite size with XRD is the Scherrer equation. This equation relates the FWHM of the diffraction peak to the crystallite size, the wavelength of the X-rays used, and the diffraction angle [52].

$$FWHM = \frac{K\lambda}{D\cos\theta},$$

where D is the crystal grain size, λ is the wavelength of X-ray, and θ is the diffraction angle. K is the Scherrer constant which is in range of 0.62–2.08. [8]

Experiment Specifications and Parameters

The XRD measurements for the five treated Niobium samples were performed on a PANalytical EMPYREAN machine. In all the measurements, a spinner sample stage was used. This sample stage has a rotational movement during the measurement to vary the x-ray angle of incidence with the sample surface. Therefore, the diffraction is the average of diffractions from the sample with different orientations. The sample holder was amorphous Silicon, since Silicon will not diffract constructively in our Bragg angle (2θ)

range of interest. The X-ray gun was set at a voltage of 45 kV and the tube current was measured at 40 mA. A total of 3046 number of point signals were measured in the Bragg angle range of $2\theta = [10,90]$.

Figure 35 - Image of the PANalytical EMPYREAN XRD machine.[5]

[5] https://www.malvernpanalytical.com/en/products/product-range/empyrean-range/empyrean

Figure 36 shows the optics settings and parameters used in the XRD measurements.

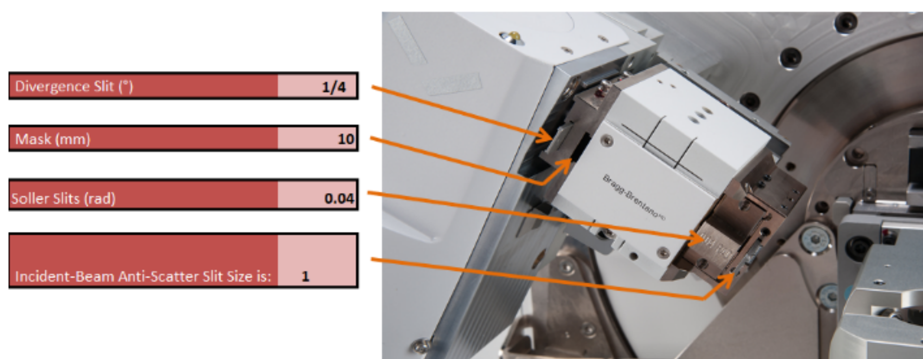

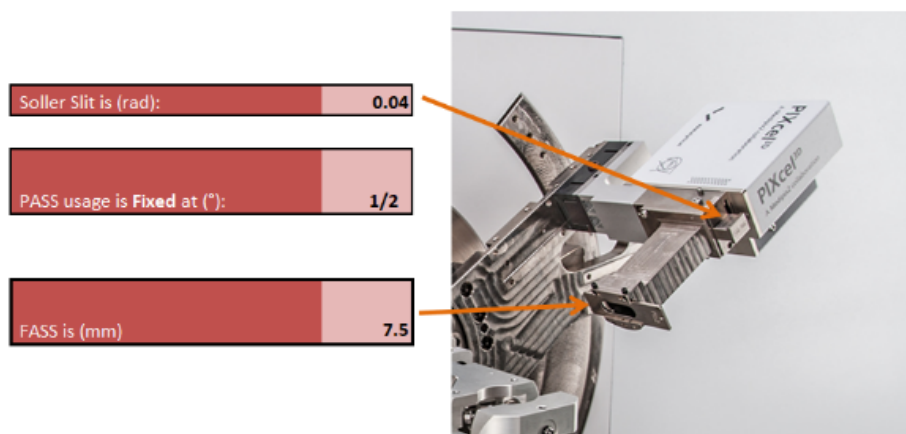

Figure 36 - The optics settings and parameters used in the XRD measurements.

The XRD signal from all five treated Niobium samples are overlaid in Figures 22 and 23. These results show three predominant peaks at Bragg angles of 39, 56, and 70

degrees, which are associated with Niobium's 011, 002, and 112 crystalline planes. The sharpness of the peaks are a measure of the material crystallinity.

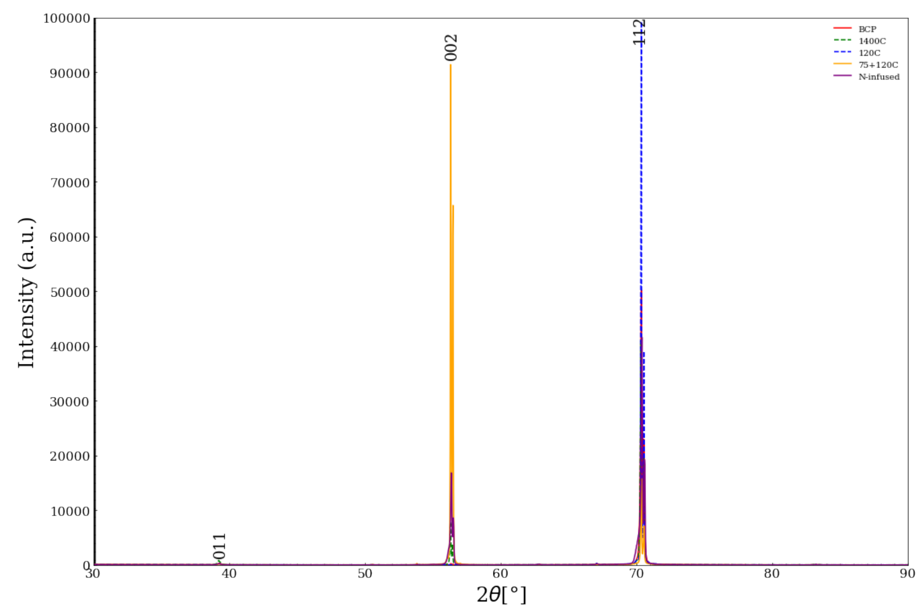

Figure 37 - The XRD signal from all five treated Niobium samples

Figure 38 shows a closer look at the intensity of the XRD results from the 5 analyzed samples, demonstrating several smaller peaks. These smaller peaks are ignored in the subsequent crystalline grain size distribution analysis.

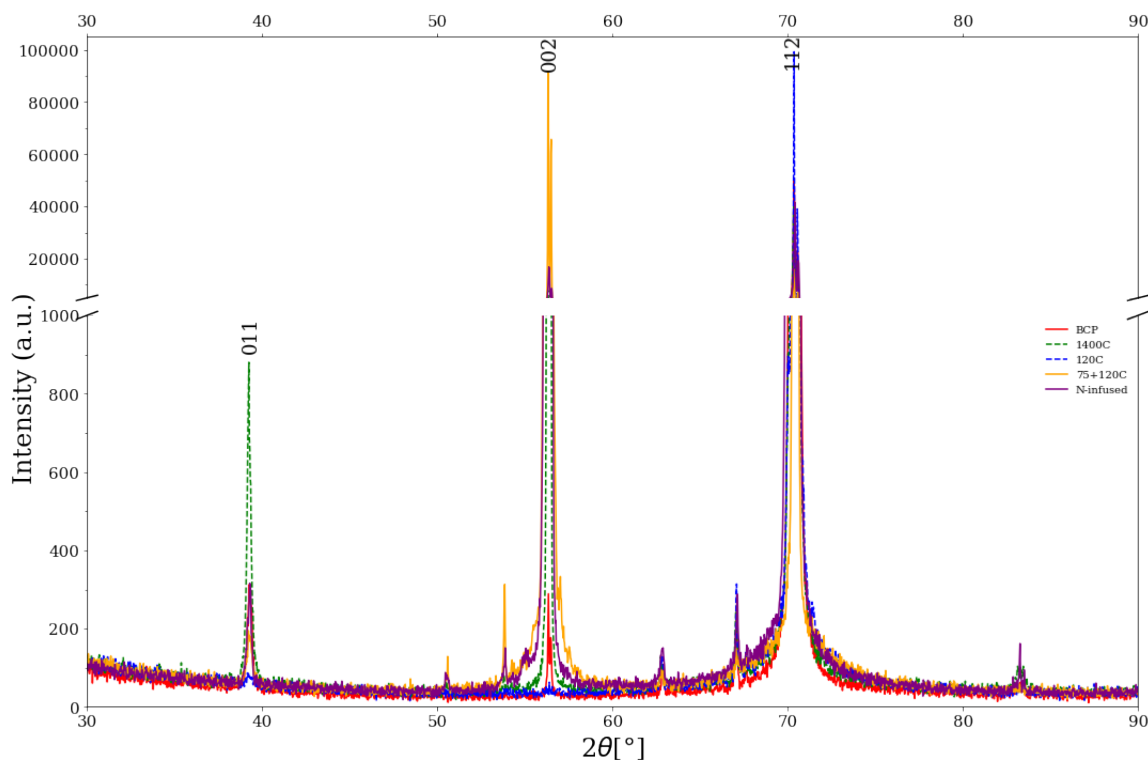

Figure 38 - The XRD signal from all five treated Niobium samples (zoomed version)

The three predominant peaks in the XRD results are individually plotted and analyzed in Figures 8 through 10. These results show a comparison of peak shapes and intensities and at the three predominant peaks (at 39, 56, and 70 degrees).

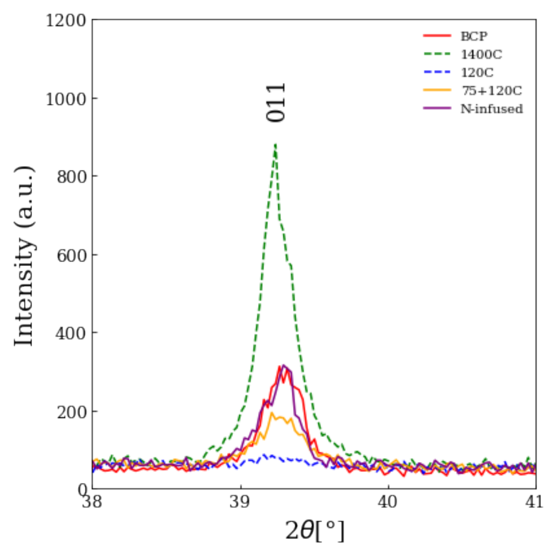

Figure 39 - Magnified scale showing the peaks near 39 degrees

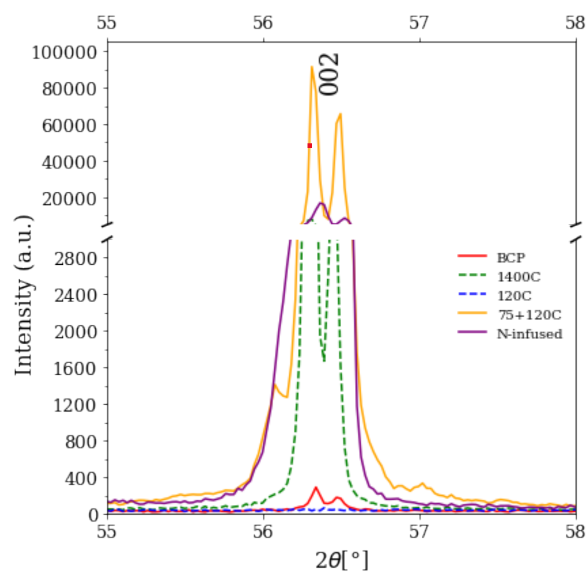

Figure 40 - Magnified scale showing the peaks near 56 degrees

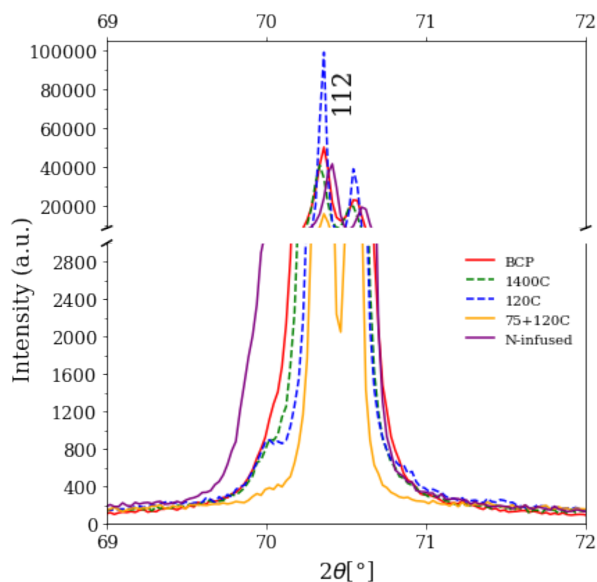

Figure 41 – Peak for all samples 70 degrees

Based on the above-presented XRD results and the Scherrer grain size calculation method, the crystalline size of the five analyzed samples are calculated and presented in Table 10 [53]. In this table, we present the sizes with more significant figures than we have confidence in (we estimate an error of ± 0.05 μm, or 1 decimal place when measured in μm, as described in section 3.3), as these numbers are used to create the averages as discussed next.

Table 10 - Crystallize size of the samples at the major Nb peaks

Sample Name	Crystallite Size [Å] at 2θ=39° hkl=011	Crystallite Size [Å] at 2θ=56° hkl=002	Crystallite Size [Å] at 2θ=70° hkl=112
BCP	599	10510	1658
1400C	680	6547	1429
120C	235	-	19321
75+120C	384	31658	19325
N-infused	1185	6579	19379

Since the 2 major peaks we have in the sample are near 56° and 70°, the average crystallite size of the materials was taken as the average crystallite size in these two peaks. For sample 120C since we do not have a peak around 56° the crystallite size calculated from peak 70° is considered as the material crystallite size. The table below shows the calculated crystallite size for the samples, where we have adjusted the presented precision of the results to reflect our estimation of error in the data which was discussed in section 3.3.

Table 11 – Average crystallite size of the samples based on the average grain size extracted from the three main peaks (39°, 56°, and 70°).

Sample Name	BCP	1400C	120C	75+120C	N-infused
Average Crystallite Size [Microns]	0.6	0.4	1.9	2.5	1.3

Appendix B - Energy Dispersive X-Ray Spectroscopy (EDS/EDX) of Bulk Sample

In order to gain insight into the material composition of the sample, an Energy Dispersive X-Ray Spectroscopy (EDS/EDX) analysis was performed.

Figure 42 shows an EDX result for an FIB cut edge of the bulk BCP sample, where we viewed the edge at angle that allowed us to also view the uppermost gold coated surface at oblique incidence. This measurement was taken with a Hitachi S-4800 FESEM machine. Figure 42(a) is a secondary electron image of the region at 20 keV. This was taken while performing EDX mapping at the long (~15 mm) working distance required for the x-ray detector insertion, and hence it is relatively low-resolution micrograph. Here, our electron beam penetrated >1 μm beneath the 100 nm thickness protective gold layer, so x-rays from Nb and O are observed in the gold coated area. The Nb and O map appears reasonably uniformly across the entire region. However, we see a slightly increase in Nb counts in the non-gold covered region and see that in comparison the O counts are more uniform over the entire region. This indicates that the oxygen signal may be dominated by overlying contamination, rather than the underlying NbO_x layer.

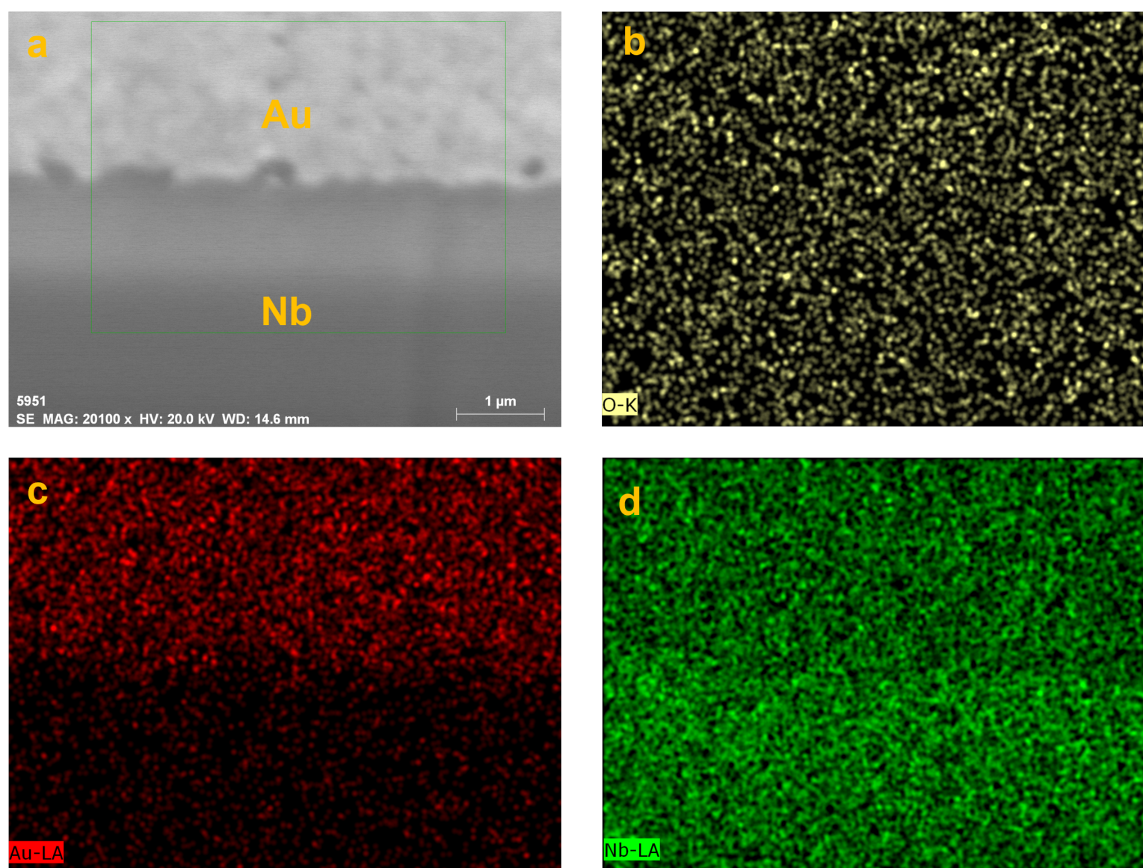

Figure 42 - (a) Secondary electron image from the Nb - Au interface and (b, c, d) EDX elemental maps of O, Au, and Nb respectively.